

## Tracer studies of pathways and rates of meltwater transport through Arctic summer sea ice

H. Eicken,<sup>1</sup> H. R. Krouse,<sup>2</sup> D. Kadko,<sup>3</sup> and D. K. Perovich<sup>4</sup>

Received 8 August 2000; revised 21 March 2001; accepted 23 July 2001; published 18 October 2002.

[1] At the Surface Heat Budget of the Arctic Ocean (SHEBA) program's field site in the northern Chukchi Sea, snow and ice meltwater flow was found to have a strong impact on the heat and mass balance of sea ice during the summer of 1998. Pathways and rates of meltwater transport were derived from tracer studies ( $\text{H}_2^{18}\text{O}$ ,  $^7\text{Be}$ , and release of fluorescent dyes), complemented by in situ sea-ice permeability measurements. It was shown that the balance between meltwater supply at the surface (averaging between 3.5 and 10.5 mm d<sup>-1</sup>) and ice permeability (between  $<10^{-11}$  and  $>10^{-9}$  m<sup>2</sup>) determines the retention and pooling of meltwater, which in turn controls ice albedo. We found that the seasonal evolution of first-year and multiyear ice permeability and surface morphology determine four distinct stages of melt. At the start of the ablation season (stage 1), ponding is widespread and lateral melt flow dominates. Several tens of cubic meters of meltwater per day were found to drain hundreds to thousands of square meters of ice through flaws and permeable zones. Significant formation of underwater ice, composed between  $<30$  and  $>50\%$  of meteoric water, formed at these drainage sites. Complete removal of snow cover, increase in ice permeability, and reductions in hydraulic gradients driving fluid flow mark stage 2, concurrent with a reduction in pond coverage and albedo. During stage 3, maximum permeabilities were measured, with surface meltwater penetrating to 1 m depth in the ice and convective overturning and desalination found to dominate the lower layers of first-year and thin multiyear ice. Enhanced fluid flow into flaws and permeable zones was observed to promote ice floe breakup and disintegration, concurrent with increases in pond salinities and  $^7\text{Be}$ . Advective heat flows of several tens of watts per square meter were derived, promoting widening of ponds and increases in pond coverage. Stage 4 corresponds to freeze-up. Roughly 40% of the total surface melt was retained by the ice cover within the ice matrix as well as in surface and under-ice ponds (with a total net retention of 15%). Based on this work, areas of improvement for fully prognostic simulations of ice albedo are identified, calling for parameterizations of sea-ice permeability and the integration of ice topography and refined ablation schemes into atmosphere-ice-ocean models. **INDEX TERMS:** 1635 Global Change: Oceans (4203); 1863 Hydrology: Snow and ice (1827); 4207 Oceanography: General: Arctic and Antarctic oceanography; 4540 Oceanography: Physical: Ice mechanics and air/sea/ice exchange processes; **KEYWORDS:** sea ice, Meltwater flow, permeability, albedo, ablation, heat budget

**Citation:** Eicken, H., H. R. Krouse, D. Kadko, and D. K. Perovich, Tracer studies of pathways and rates of meltwater transport through Arctic summer sea ice, *J. Geophys. Res.*, 107(C10), 8046, doi:10.1029/2000JC000583, 2002.

### 1. Introduction

[2] The Arctic's role in the global climate system is significantly influenced by the presence of a perennial

sea-ice canopy, covering approximately  $6 \times 10^6$  km<sup>2</sup> or 80% of the Arctic Ocean. Seasonal ice melt and retreat along the perimeter of the perennial pack ice figure prominently in the context of the Arctic Ocean's heat budget and the impact of ice-albedo feedback mechanisms on climate variability and change [Curry *et al.*, 1995; Perovich *et al.*, 1999a]. The freshwater volume generated through seasonal ice melt over the marginal seas is roughly equivalent to that resulting from surface melt of ice in the Arctic Basin. Surface ablation of perennial ice on average accounts for the removal of 0.3 to 0.7 m of ice each summer [Untersteiner, 1990; Romanov, 1995; Golovin *et al.*, 1996]. Despite the importance of this phenomenon, we are cur-

<sup>1</sup>Geophysical Institute, University of Alaska, Fairbanks, Alaska, USA.

<sup>2</sup>Department of Physics and Astronomy, University of Calgary, Calgary, Alberta, Canada.

<sup>3</sup>Rosenstiel School of Marine and Atmospheric Sciences, University of Miami, Miami, Florida, USA.

<sup>4</sup>Cold Regions Research and Engineering Laboratory, Hanover, New Hampshire, USA.

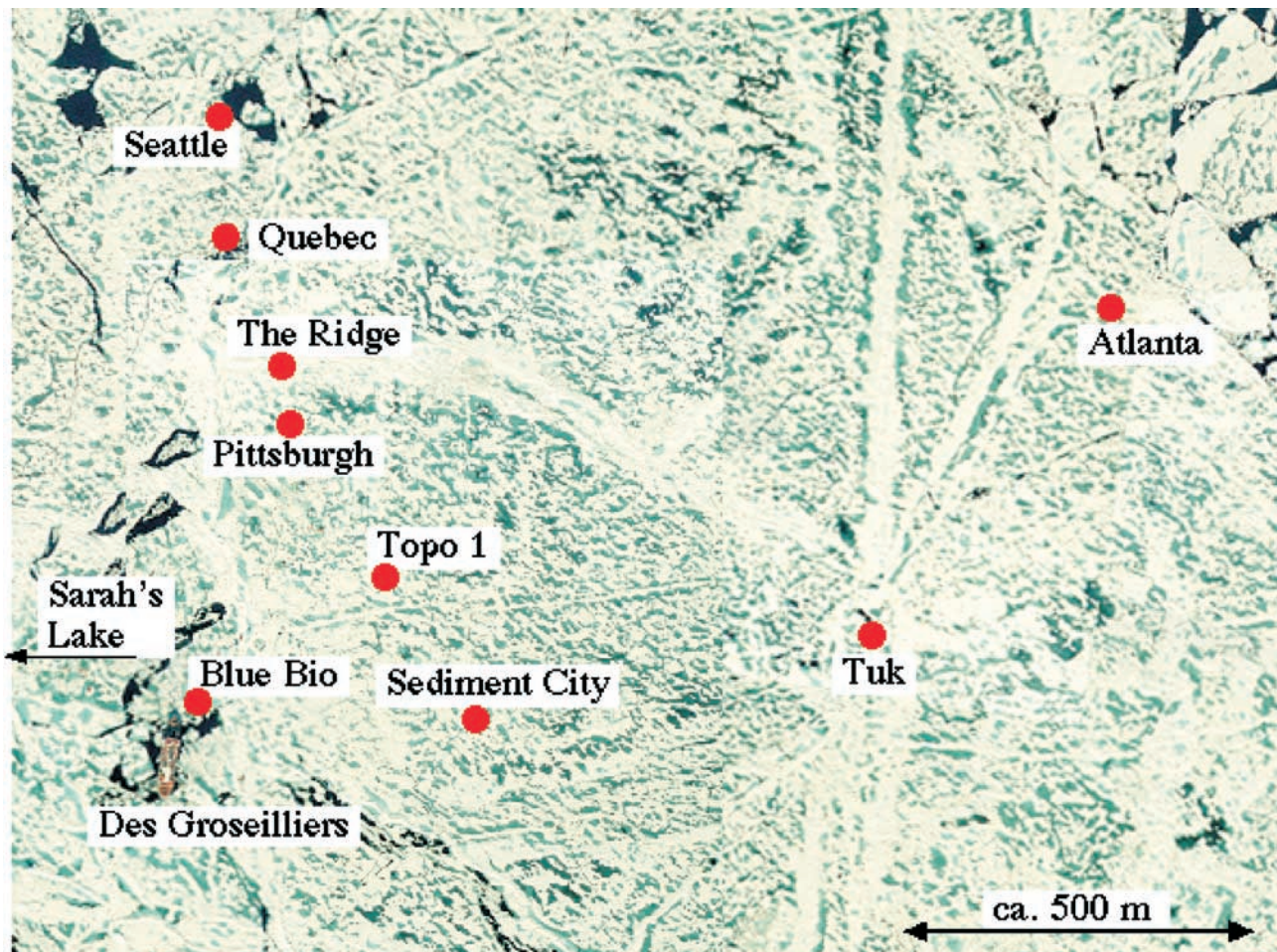


**Figure 1.** Aerial photomosaic of the SHEBA field site (25 July 1998). The lead site “Sarah’s Lake” is approximately 1 km to the left of the image. At this advanced stage of summer melt, ponds cover more than 20% of the ice surface with pond ice significantly thinned or partially melted through (e.g., three triangular ponds in FY ice to the lower left of Pittsburgh). Drainage of meltwater from ridge flanks results in higher albedo of ridged ice.

rently lacking quantitative estimates of the retention of surface meltwater during the ablation season and its impact on the evolution of the sea-ice cover.

[3] In principle, meltwater can be diverted into various reservoirs. Most important is its pooling in surface melt ponds, typically covering between 20 and 50% of the ice surface at the peak of melt (Figure 1) [Eicken *et al.*, 1996; Fetterer and Untersteiner, 1998; Tschudi *et al.*, 2001; Perovich *et al.*, 2002]. The large-scale albedo of ponded ice ranges between 0.35 and 0.6, a critical reduction compared to that of 0.65 for bare white ice [Maykut, 1986; Perovich *et al.*, 2002]. Downward percolation of meltwater into the porous ice matrix has been shown to drastically reduce surface salinities of Arctic multiyear ice [Untersteiner, 1968], strongly affecting the thermal and optical properties of summer sea ice [Perovich, 1998; Bitz and Lipscomb, 1999]. Meltwater discharged through highly permeable ice or flaws and along floe margins contributes to the freshwater flux at the ocean surface [Kadko, 2000]. It can also be retained under thin ice or in bottom depressions, with underwater ice (“false bottoms”) forming at the freshwater-seawater interface [Untersteiner and Badgley, 1958; Martin and Kauffman, 1974; Eicken, 1994].

[4] The redistribution of surface meltwater is hence of critical importance for the ice energy and mass balance as it impacts ice albedo and heat fluxes through the ice cover. In addition, meltwater retention can affect the salt and heat balance of the mixed layer [Kadko, 2000]. Owing to its low salinity and low nutrient concentrations, meltwater mostly retards ice-associated biological production, although enhancement of algal growth has also been reported for under-ice meltwater lenses [Gradinger, 1996]. The fate of snow meltwater determines the transfer of atmospheric pollutants into the ocean or to the sea-ice ecosystem [Lange and Pfirman, 1998].

[5] Despite the importance of ablation processes, little is known about the fate of the meltwater generated during the course of the summer. While long-term net salt fluxes resulting from ice growth and melt have been derived from oceanographic tracer measurements [Östlund and Hut, 1984; Bauch *et al.*, 1995], neither origin nor seasonal evolution of the meltwater signal has been studied in much detail. Both, western and Russian scientific drifting stations included observations of surface melt. After the initial thrust in the 1950s [e.g., Untersteiner and Badgley, 1958], little additional work has been done in the North American



Arctic. Russian researchers have completed comprehensive, routine measurements of ice ablation at numerous North Pole (SP) Drifting Stations, but to the best of our knowledge (which, admittedly, is limited by language and other constraints) this work mostly focused on bulk ablation processes [e.g., *Nazintsev*, 1963, 1971; *Appel*, 1988; *Golovin et al.*, 1996]. Similarly, whereas the areal melt pond coverage and its impact on ice albedo has received considerable attention [*Maykut*, 1986; *Appel*, 1988; *Eicken et al.*, 1996; *Fetterer and Untersteiner*, 1998; *Tschudi et al.*, 2001; *Perovich et al.*, 2002], much less is known about the hydrological processes that determine onset and seasonal evolution of ponding.

[6] The current study is motivated by the lack of such data. It is furthermore driven by the hypothesis that (1) the evolution and mass balance of the perennial Arctic ice pack are significantly affected by sea-ice hydrological processes and (2) the macroscopic ice properties, in particular permeability, in conjunction with ice topography and flaw occurrence determine the redistribution and ultimate fate of snow and ice meltwater generated during summer. Representing the ice cover as a two-dimensional, isotropic medium saturated with an unconfined fluid, Darcian meltwater flow through the ice is described by

$$\nabla[hk \nabla h] + q = n_l \frac{\partial h}{\partial t}, \quad (1)$$

where  $k$  is the intrinsic permeability and  $n_l$  the fluid porosity (i.e., brine volume fraction) of the ice,  $h$  the hydraulic head and  $q$  the meltwater source function per unit area [*Freeze and Cherry*, 1979]. The position of the water table within ice or ponds hence largely depends on the surface melt rate and the permeability of the underlying ice. It is mostly the hydraulic gradient in combination with the permeability structure that determines the lateral transport of surface meltwater into ponds, cracks or leads. Sea-ice properties  $k$  and  $n_l$  as well as the ablation rate in equation (1) vary significantly during the course of summer. This should affect the seasonal evolution of the meltwater pool associated with the sea-ice cover.

[7] The Surface Heat Budget of the Arctic Ocean (SHEBA) Project provided an ideal opportunity to study the hydrology of summer sea ice at a drifting station in the northern Chukchi Sea and the adjacent Arctic Ocean in 1998 [*Perovich et al.*, 1999a]. At the SHEBA field site, which comprised both first- and multiyear ice of different age and morphology, processes and pathways of meltwater redistribution were studied through the combination of in situ permeability measurements and the release of fluorescent dyes, complemented by measurements of stable ( $H_2^{18}O$ ) and transient ( $^7Be$ ) isotopic tracers to quantify the flux of snow and ice meltwater through the system. An ice mass balance program provided data on surface ablation rates [*Perovich et al.*, 1999a], supplemented by ice topography and noninvasive thickness measurements [*Eicken et al.*, 2001].

[8] One of the overarching themes of the SHEBA program is the study of ice-albedo feedback mechanisms and the concurrent improvement of sea-ice models required to adequately address these problems [*Moritz et al.*, 1993]. The albedo and the mass balance of summer sea ice

strongly depend on the amount of meltwater retained at the surface in ponds, percolating into the ice matrix or refreezing at the floe bottom. Rather than prescribing the impact of these processes, e.g., by assigning a constant or temporally variable melt pond fraction, the next generation of sea-ice models [e.g., *Curry et al.*, 1995; *Schramm et al.*, 1997; W. Lipscomb, unpublished data, 2000] will have to include prognostic ice-hydrology components in order to adequately represent the variable ice albedo in potential feedback loops. The present study may help improve our insight into the nature and importance of the underlying processes.

## 2. Background and Methods of Data Acquisition and Analysis

### 2.1. Study Area

[9] During the course of this study from late May to mid-August 1998, Ice Station SHEBA drifted between 76 and 78.5°N and 160 and 170°E in the northern Chukchi Sea [*Perovich et al.*, 1999a]. The experiments and measurements described in this contribution were mostly carried out over a core area of approximately 2 km<sup>2</sup> (Figure 1), composed of a mixture of multiyear (MY) and first-year (FY) ice, the latter mostly in the form of refrozen leads. Detailed descriptions of the individual measurement sites are provided by *Perovich et al.* [1999b].

### 2.2. Measurements of Sea-Ice Topography, Properties, and Ablation Rates

[10] Changes in surface topography (elevation of pond, ice or snow surface, depth of melt ponds) were recorded with a laser-leveling device (maximum error <10 mm relative to sea level). Most locations were revisited every two to four weeks, with topography and indirect ice thickness measurements along two profiles (<100 m long with 0.5 m horizontal spacing) completed at five- to ten-day intervals [*Eicken et al.*, 2001]. Changes in pond water levels were recorded with a float-gauge installed in a stilling well and mounted on a shaded platform grounded at a fixed depth level (1 m) in the ice.

[11] Ice cores were obtained with a 10-cm fiberglass-barrel CRREL-type corer. Immediately after coring, the core was photographed and the ice temperature was determined by drilling holes to the center of the core and inserting a thermistor probe (accuracy better than 0.2 K). Cores were then sectioned into 5- or 10-cm segments at the drilling site to minimize loss of brine and transferred into sealed plastic containers. Salinities of melted samples were obtained through electrolytic conductivity measurements with a YSI model 30 sonde (measurement error <0.02 or <1% of the bulk salinity, whichever is larger). Some melted core samples were transferred into glass bottles for stable isotope measurements (see below). In situ brine volumes were derived from the ice salinity and temperature measurements and estimates of ice density based on data sets for Arctic FY and MY ice by *Eicken et al.* [1995] as described by *Leppäranta and Manninen* [1988] for the temperature interval between -2 and 0°C.

[12] Top and bottom ablation rates of sea ice were obtained at 135 locations, mostly at 2-day intervals, as part of the SHEBA ice mass balance program [*Perovich et al.*,

1999a, 1999b]. Here, a subset representative of the ice types comprising the sampling locations has been analyzed.

## 2.3. In Situ Permeability Measurements

### 2.3.1. Outline of Method

[13] Despite its importance in determining the evolution of meltwater layers at the surface of Arctic summer sea ice, very little is known about the magnitude and variability of ice permeability. Here, a method commonly employed in hydrogeological applications, the so-called slug or bail test, has been adapted to the ice environment. We only provide a brief overview of the method, with a more detailed account given by Freitag [1999] and Freitag and Eicken (Melt water circulation and permeability of Arctic summer sea ice derived from hydrological field experiments, submitted to *Journal of Glaciology*, 2001, hereinafter referred to as Freitag and Eicken, submitted manuscript, 2001). According to Darcy's law, the intrinsic permeability or hydraulic conductivity of a medium is defined as the constant of proportionality that relates the effective pressure gradient  $\nabla P$  to the specific discharge  $\mathbf{v}$  (the fluid velocity averaged over the entire cross section of the flow):

$$\mathbf{v} = -\frac{\mathbf{K}}{\mu} \nabla P, \quad (2)$$

where  $\mathbf{K}$  is a tensor of second order and  $\mu$  is the fluid's dynamic viscosity [Freeze and Cherry, 1979]. While the classic Darcy experiment is conducted on a laboratory sample of the porous medium, slug or bail tests are carried out in situ. Here, 14-cm diameter holes were drilled to a given depth level, the core was removed and a packer (a metal tube with an inflatable outer rubber jacket, pressing against the hole wall) inserted to limit the influx of water into the hole to that passing through its bottom surface with cross-sectional area  $A$  of 154 cm<sup>2</sup>. An ultrasonic transducer measured the water level  $h$  within the hole at a sampling rate of <10 Hz. As  $dh/dt$  describes both the rate of change in hydraulic head driving the flow and the influx of water into the hole, equation (2) can be integrated to yield the permeability in the vertical  $z$ -direction  $k_z$  according to

$$h(t) = h(t_0) \exp\left(-k_z \frac{g\rho}{\mu L} t\right), \quad (3)$$

with gravitational acceleration  $g$ , fluid density  $\rho$  and  $L$  the thickness of the underlying ice layer. As the ice cover exhibits a finite permeability in  $x$ - and  $y$ -direction, flow into the hole is not limited to the  $z$ -component. Freitag [1999] has derived analytical functions to correct for this effect. Based on two-dimensional modeling, the permeability  $k_z$  has to be adjusted, dividing by  $\gamma(L)$  based on the ratio between fluid flow into the hole with laterally permeable ( $k_{x,y} > 0$ ) and impermeable ( $k_{x,y} = 0$ ) ice:

$$\gamma(L) = 0.17 + 10.7L, \quad (4)$$

for  $k_{x,y} = 0.1 k_z$  as based on lab measurements of the permeability of Arctic summer sea ice along the three principal axes [Freitag, 1999; J. Freitag and H. Eicken, submitted manuscript, 2001].

### 2.3.2. Errors and Uncertainties

[14] The permeability measurements are affected by three main sources of error. Ultrasonic distance measurements (accurate to better than  $\pm 2$  mm) and fitting of exponential curves to the water level data (typically more than 95% of the variance explained by the regression model) result in a cumulative error estimated at <10%. Insufficient sealing of the outside perimeter results in an overestimation of the specific discharge into the hole. In the most problematic cases of deep holes (large surface area, large hydraulic gradients) and in the presence of flaws, the maximum flow increase is estimated at 50%, overestimating permeability by a factor of 1.5. Finally, to correct for anisotropic flow into the hole due to smaller permeabilities in the horizontal as compared to the vertical direction, it is assumed that  $k_{x,y} = 0.1 k_z$  (equation 4) based on triaxial permeability measurements of Arctic sea ice. Deviations from this value will strongly affect the derived permeabilities. Thus, for an 0.5 m thick ice layer and  $k_{x,y} = 0.01 k_z$ , computed  $k_z$  are smaller by a factor of 2.7 compared to the standard case and for  $k_{x,y} = k_z$  they are larger by a factor of 3.0. As the overall structure of the level ice at the SHEBA site was fairly uniform and mostly composed of columnar ice, uncertainties concerning the magnitude of this correctional factor are deemed to result in a systematic error rather than increasing the variance. In summary, the absolute accuracy of the permeability measurements is estimated as  $\pm 150\%$  in the worst case, and as <50% excluding uncertainties in the determination of  $\gamma(L)$ . Given that permeabilities span more than two orders of magnitude during the course of the season, these uncertainties are acceptable.

## 2.4. Tracer Studies

### 2.4.1. Fluorescent Tracers

[15] In studying meltwater transport, salinity is only of limited use as a proxy parameter, because the salinity of the fluid within the ice matrix and in melt ponds varies considerably. Also, freshening of the mixed layer as such does not provide any indication of the origin of the meltwater. A major aim of the present study is to utilize both natural and artificial tracers in following the passage of meltwater. For a direct release into the ice matrix or a melt pond, two fluorescent tracers, fluoresceine (FLC, C<sub>20</sub>H<sub>10</sub>O<sub>5</sub>Na<sub>2</sub>) and sulforhodamine B (SRB, C<sub>27</sub>H<sub>29</sub>O<sub>7</sub>N<sub>2</sub>S<sub>2</sub>Na), are particularly suited owing to their detectability at very low concentrations down to approximately  $5 \times 10^{-6}$  mg l<sup>-1</sup>, their stability and inertness in the presence of ice surfaces. A more detailed assessment of their utility in geoscience and glaciological studies can be found in Käss [1992] and Freitag [1999]. Here, known amounts of the tracer (typically between 250 and 1000 mg) were released into 5-cm diameter boreholes or melt ponds after deployment of an array of samplers to monitor dispersion of the tracer as a function of time. In monitoring flow through networks of connected melt ponds with low meltwater residence times, the tracer front was also tracked visually. Exposed to direct sunlight, FLC dissociates with a half-life of more than 6 hours [Freitag, 1999]. While this does not impact studies of the tracer front, longer-term dispersion experiments were mostly conducted with photochemically stable SRB. Concentrations were measured with a Shimadzu RF1501 spec-

trofluorometer, buffering the sample to a pH of 8.0, at excitation and emission wavelengths of 491 and 512 nm for FLC and 564 and 583 nm for SRB. Calibration was carried out at the start and end of the field campaign against a dilution series of fresh stock solutions. For FLC, a linear relationship between concentration and fluorescence signal was observed in the concentration range  $5 \times 10^{-6}$  to  $1 \text{ mg l}^{-1}$ , for SRB between  $5 \times 10^{-4}$  and  $1 \text{ mg l}^{-1}$ . For longer-term studies of vertical tracer movement through the ice cover, rhodamine B (RB,  $\text{C}_{28}\text{H}_{31}\text{ClN}_2\text{O}_3$ , excitation and emission wavelengths of 555 and 580 nm) was employed since it is adsorptive, resulting in longer residence times in the ice matrix [Käβ, 1992; Krembs *et al.*, 2000]. RB is particularly suited for core sampling of flow fields, as the loss of tracer from the ice matrix upon sample extraction is greatly reduced.

#### 2.4.2. Stable Isotope Measurements

[16] Snowmelt typically accounts for less than a third of the total surface ablation, with most of the snow cover removed by late June on Arctic Ocean sea ice [Yanes, 1962; Perovich *et al.*, 1999a]. Owing to the strong contrasts in the isotopic composition of snowmelt and seawater or sea ice, with the former highly depleted in  $^{18}\text{O}$  and D, the passage of meteoric water can be traced through the sea-ice system based on stable isotope measurements. The inventory of  $^{18}\text{O}$  in snow, sea ice, ponds and brine was determined at regular intervals throughout the course of summer. Concentrations of  $^{18}\text{O}$  were measured at the Stable Isotope Laboratory, Department of Physics and Astronomy, University of Calgary, on a VG 903 mass spectrometer (carbon dioxide equilibration, measured against VSMOW) at a precision of better than 0.4 ‰. Data are reported in the  $\delta^{18}\text{O}$  notation, with

$$\delta^{18}\text{O}(\text{samples}) = \left[ \frac{\left( \frac{^{18}\text{O}}{^{16}\text{O}} \right)_s}{\left( \frac{^{18}\text{O}}{^{16}\text{O}} \right)_{\text{VSMOW}}} - 1 \right] \cdot 1000\text{‰}. \quad (5)$$

#### 2.4.3. $^7\text{Be}$ Measurements

[17]  $\text{Be-7}$  is a cosmic ray produced radioactive nuclide with a radiodecay half-life of 53.3 days. It is deposited upon the earth's surface by precipitation and is homogenized within the surface mixed layer of the ocean rapidly with respect to its decay rate [Silker, 1972; Young and Silker, 1980; Kadko and Olson, 1996]. In snow, the  $^7\text{Be}$  activity (equivalent to concentration, here expressed as disintegrations per minute per  $\text{m}^3$ , or  $\text{dpm m}^{-3}$ ) is approximately two orders of magnitude greater than in the ocean mixed layer, because a given  $^7\text{Be}$  flux is diluted in mixed layers typically tens of meters deep, but deposited in snow layers which are at least an order of magnitude shallower, thereby concentrating the nuclide relative to the surface ocean [e.g., Cooper *et al.*, 1991]. The average depositional flux at the SHEBA site during July and August 1998 was  $120 \text{ dpm m}^{-2} \text{ d}^{-1}$  [Kadko, 2000].

[18] In this work, approximately 20 L samples of water were collected from three selected melt ponds in a time series during the summer field season. In addition, meltwater samples were extracted from the ice matrix in holes drilled to different depths. To these samples 0.5 mL of concentrated HCl and stable Be yield tracer were added

[e.g., Dibb, 1990]. The  $^7\text{Be}$  was removed by coprecipitation with iron-hydroxide, dried, and counted by gamma spectrometry. The  $^7\text{Be}$  has a readily identifiable peak at 478 keV, and the counting system was calibrated by preparing a commercial standard in geometries identical to the samples. The stable Be in the precipitate was then measured by atomic absorption to calculate the  $^7\text{Be}$  recovery during precipitation.

#### 2.4.4. Errors and Uncertainties

[19] For fluorescent tracer studies, errors are largest at low concentrations, with maximum deviations between calibration functions and measured data points ranging between 70 and 130% at concentrations of  $10^{-4} \text{ mg l}^{-1}$  and increasing up to a factor of 13 for concentrations below  $10^{-5} \text{ mg l}^{-1}$  (with highest errors for RB and lowest for FLC). At concentrations of  $10^{-3} \text{ mg l}^{-1}$  and above, maximum deviations are below 25%. Since most data for quantitative assessments of volume fluxes and locations of tracer fronts were obtained at concentrations  $\geq 10^{-3} \text{ mg l}^{-1}$ , only assessments in the low-permeability regime or for experiments extending over prolonged periods of time are affected by higher uncertainties of up to 50% in extreme cases. The use of tracers for direct tracking of fronts in measurements of specific discharge (section 3.4) is not affected by the sensitivity of the method. It is mostly the uncertainty in cross-sectional area and average velocity that compromises measurements. While the maximum absolute error is estimated to be <50%, the morphology and hydrology of the drainage basin is only gradually changing over time, such that the relative error for measurements reported in section 3.4 is considerably smaller. This is supported by direct comparisons with mass balance measurements of the total runoff.

[20] Due to the high precision of stable isotope measurements (better than 0.4 ‰), the error in determining the fraction of meteoric water is generally <5% and at maximum 10% for samples collected late in the season. Hence, the accuracy in the determination of percolation fronts is mostly controlled by the sample resolution (0.05 m). Precision of  $^7\text{Be}$  measurements is determined by the statistical counting error and uncertainty in the blank sample data. With generally high activities in pond and ice samples, the total error averages at 6.5% and ranges between 2.5 and 44%.

### 3. Results

#### 3.1. Ablation Rates and Meltwater Production

[21] The total surface ablation for the SHEBA site during the summer of 1998 amounted to 0.60 m (water equivalent, WE, based on an ice density of  $910 \text{ kg m}^{-3}$  [Perovich *et al.*, 1999b]). This includes complete removal of the 0.34 m deep snow cover (density taken as  $300 \text{ kg m}^{-3}$ ). Bottom ablation averaged at 0.45 m (WE) over the whole summer, extending well into September [Perovich *et al.*, 1999b]. The cumulative snow and ice ablation is shown in Figure 2 for a number of gauges representative of the main ice types. At these sites, the total average surface ablation amounts to  $0.66 \pm 0.13 \text{ m}$  (WE). During the period of surface melt, between 27 May (day 147) and 21 August (day 233), bottom ablation for this subset of all the data amounted to  $0.37 \pm 0.19 \text{ m}$  (WE).



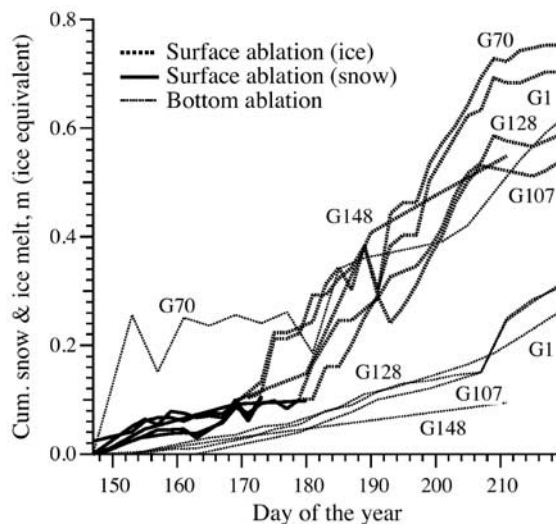


**Figure 2.** Cumulative snow and ice ablation at representative mass balance gauges at the SHEBA site for 1998 (G1: level MY ice at Seattle; G22: melt pond in MY ice along main line; G70: heavily ridged ice at the ridge; G107: level MY ice at Tuk; G128: level MY ice at Atlanta; G148: level FY ice at Baltimore). Snow ablation data have been converted to ice equivalent based on a snow density of  $300 \text{ kg m}^{-3}$ . Decreases in ablation data can result from snowfall, shifting of blocks in deformed ice (e.g., G70) and erroneous measurements.

[22] With  $3.5 \pm 0.6 \text{ mm d}^{-1}$  (WE), meltwater production is much lower during the period of snowmelt (Figure 2) than for surface ice ablation, averaging at  $10.5 \pm 2.5 \text{ mm d}^{-1}$  (WE). Surface ablation is highly variable, with the highest rates found in ponded and ridged ice. Qualitatively, this is consistent with data from Russian drift stations in the Eurasian Arctic, although mean surface and bottom ablation are somewhat lower with 0.46 and 0.23 m (WE), respectively [Golovin *et al.*, 1996].

### 3.2. Permeability Measurements and Tracer Studies of Permeability

[23] The results of permeability measurements in level FY and MY ice in horizons between 0.25 and 1.7 m depth are shown in Figure 3. Permeability  $k$  varies over more than two orders of magnitude as the melt season progresses. In early June, permeabilities were so low as to render measurements impossible (the lower threshold is taken as  $6 \times 10^{-12} \text{ m}^2$ , corresponding to less than 0.1 m rise in water level in a 1 m deep hole in 2 m ice with 0.2 m freeboard in a period of 15 min.). The transition between the low- and intermediate permeability regime occurred during a period of about a week. Due to equipment failure, no data are available for this time period. Despite the significant scatter, which is mostly due to variability in small-scale ice structure, a trend toward increases in permeability with time is apparent. FY ice exhibits slightly larger permeabilities and an earlier increase in magnitude than MY ice. The overall geometric mean of  $k = 2.0 \times 10^{-10} \text{ m}^2$  is lower than permeabilities

measured in Eurasian Arctic MY and warm FY ice at the peak of summer in 1995 and 1996 (geometric means of  $4.0 \times 10^{-10} \text{ m}^2$  and  $8.0 \times 10^{-10} \text{ m}^2$ , respectively [Freitag, 1999; Freitag and Eicken, submitted manuscript, 2001]). The geometric mean for the SHEBA data collected after 5 July is higher, amounting to  $4.0 \times 10^{-10} \text{ m}^2$ . Compared to a wider data set of lab and in situ measurements compiled by Freitag [1999], the data set falls into the intermediate permeability range.

[24] The retention of meltwater at the ice surface depends strongly on the permeability in the uppermost decimeters, which is not easily measured using the in situ technique described above. While they cannot provide absolute quantitative information, tracer dispersion measurements can help assess the permeability evolution in the upper ice layers. Figure 4 shows the results of two dispersion experiments, both conducted in level, homogeneous MY and FY ice in the absence of measurable hydraulic gradients. After releasing 100 mg of SRB and 250 mg of FLC in a hole of 0.4 to 0.5 m depth and 0.05 m diameter, tracer concentration was measured at regular intervals in the center and neighboring holes drilled to the same depth prior to the experiment. During early melt, transport was negligible, with the concentration maximum shifting by less than 0.05 m into the surrounding ice after 29 hours. In contrast, during the latter half of the melt season, permeabilities were large enough to allow for significant flow, with the tracer maximum advected by more than 0.3 m during the course of 4 hours (Figure 4, right). Conducted under comparable boundary conditions in the same ice type, such tracer experiments can indicate relative changes in permeability. Assuming nondivergent flow from the release point to the

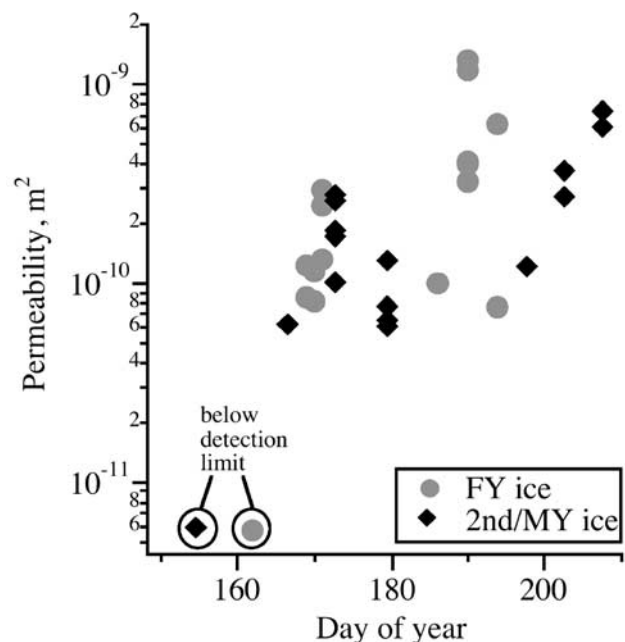


**Figure 3.** Sea-ice permeability as determined through in situ measurements during the course of the summer within level ice at depths between 0.25 and 1.70 m. At the start of the melt season, permeabilities did not exceed the detection limit of roughly  $6 \times 10^{-12} \text{ m}^2$ .

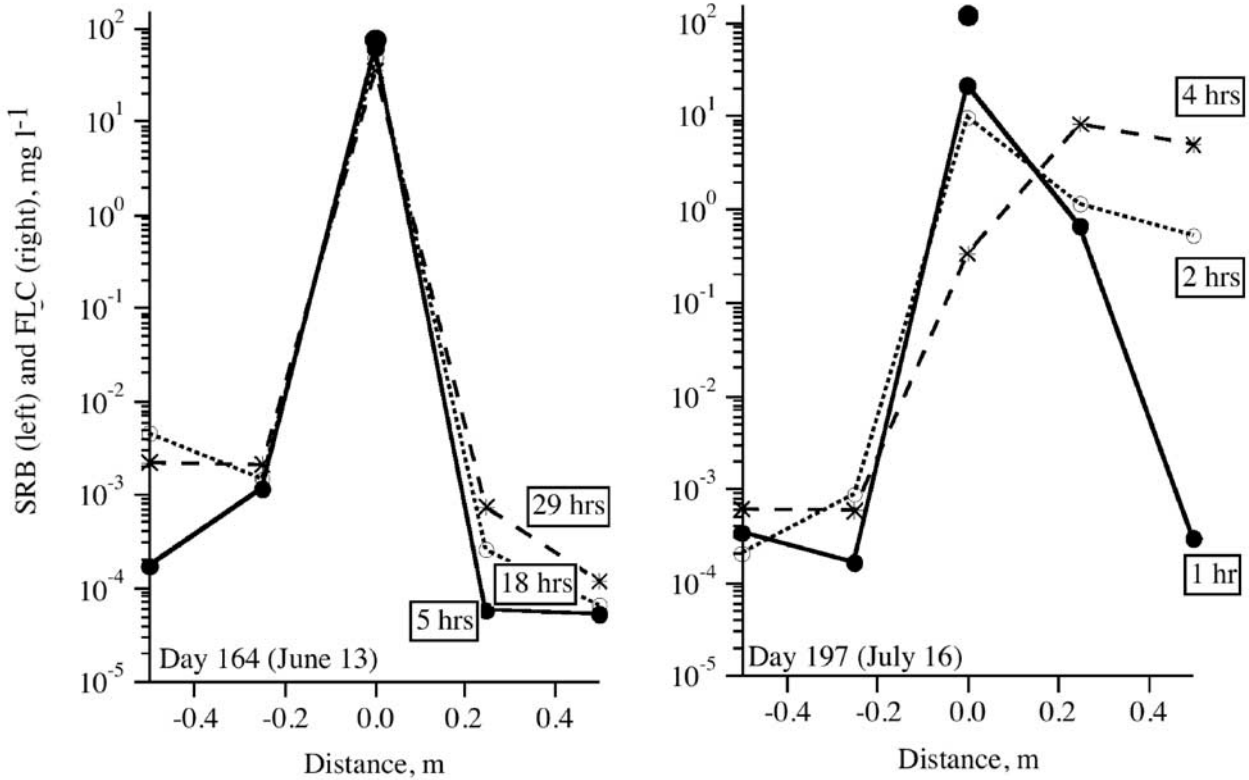


**Figure 4.** Dispersion of tracer from cylindrical hole (0.4–0.5 m deep, homogeneous tracer distribution at start of experiment) through uppermost layer of level sea ice (MY ice at main camp at left, FY ice at Sarah's Lake at right). Data have been averaged for sets of holes upstream and downstream of the prevailing direction of flow. Note different timescales for duration of experiments.

sampling hole downstream, an approximate estimate of the ratio of permeabilities  $k_1/k_2$  for two experiments can be obtained by rearranging equation 2 to

$$\frac{k_1}{k_2} = \frac{n_{l,1} \Delta r_1 \Delta t_2}{n_{l,2} \Delta r_2 \Delta t_1}, \quad (6)$$

where  $n_l \Delta r / \Delta t$  corresponds to the specific discharge through the cross section of the hole. For an effective ice porosity  $n_{l,1} = 0.052$  (day 164, derived from temperature and salinity data) and  $n_{l,2} = 0.105$  (day 197) and  $r$  and  $t$  obtained as outlined above,  $k_1/k_2$  amounts to 0.011. For  $k_2 = 4.0 \times 10^{-10} \text{ m}^2$ , corresponding to the geometric mean permeability during the latter half of the ablation period, the permeability of the upper layer on day 164 amounts to  $k_1 = 4.4 \times 10^{-12} \text{ m}^2$ , which is in good agreement with the data shown in Figure 3.

### 3.3. Hydraulic Gradients Driving Fluid Flow

[25] As outlined in section 2.3, the specific discharge through an ice surface is proportional to the product of ice permeability and hydraulic or effective pressure gradient. In summer Arctic sea ice, the latter is mostly determined by differences in hydraulic head that develop as a result of melt over a nonuniform ice surface. Other forces driving flow, such as fluid drag, have also been observed, both during the SHEBA experiments and elsewhere (Freitag and Eicken, submitted manuscript, 2001), but are generally much smaller. In the case of sea ice, the total hydraulic head is

controlled by the pressure head  $p/\rho$  since the contribution by finite flow velocity and frictional forces is small and can be ignored. Untersteiner [1968] has identified the head associated with meltwater produced at the ice surface and percolating downward into the ice as the major factor in determining the desalination of MY ice. As shown below, the pressure head associated with elevated ponds or meltwater produced above sea level also drives lateral flow over great distances.

[26] As the effective hydraulic head depends on both the production of meltwater at the ice surface and the permeability of the underlying ice, it is likely to vary considerably with the progression of the ablation season. This is confirmed by water level measurements in different types of melt ponds, providing an estimate of the evolution of hydraulic head (Figure 5a). While most of the ponds in level, undeformed sea ice exhibit maximum elevations of around 0.2 m above sea level (asl), they can exceed 0.5 m asl in ridged ice. For the majority of level-ice ponds, hydraulic head decreases to zero as season progresses. After about day 200 (19 July), only ponds in ridged or deformed ice remained well above sea level (e.g., the upper curve in Figure 5a). The decrease in pond water level is mostly explained by the seasonal increases in ice permeability by about one order of magnitude between days 170 and 200 (Figure 3).

[27] While surface melt rates subside somewhat after about day 200, the impact on the melt pond water budget

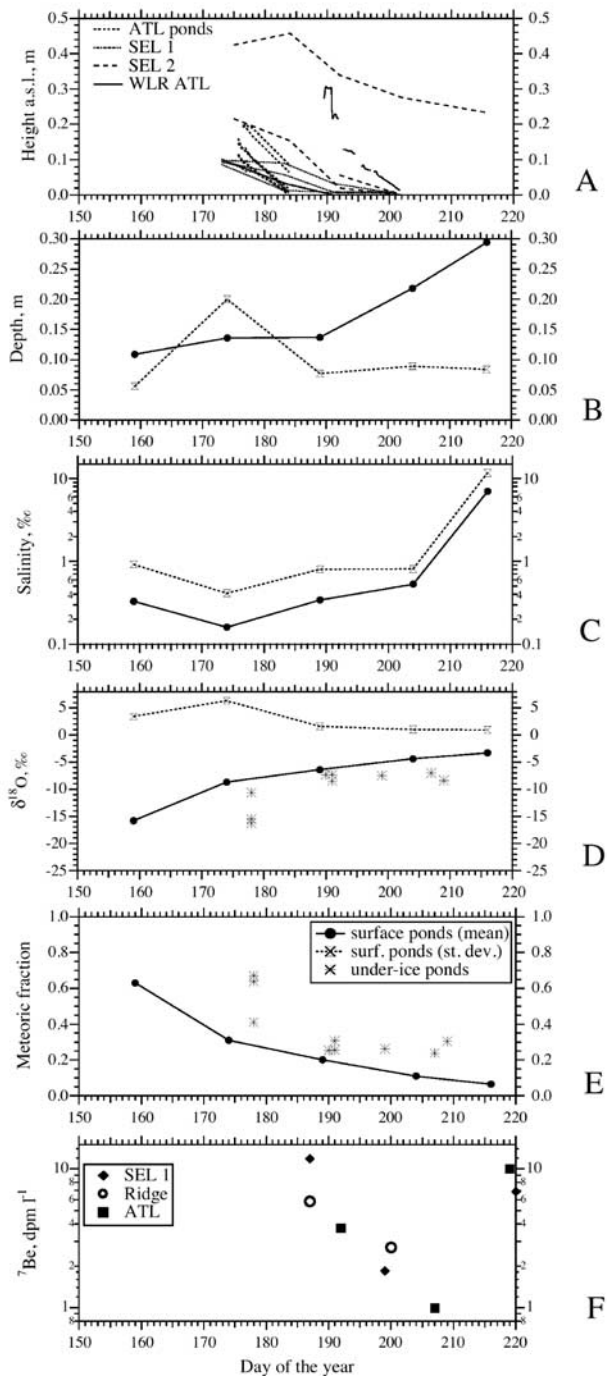


**Figure 5.** Time series of parameters related to melt pond evolution: melt pond water level relative to sea level (a), depth (b), salinity (c),  $\delta^{18}\text{O}$  of pond water (d), fraction of meteoric water derived from the isotopic composition (e), and  $^7\text{Be}$  concentration for three representative ponds (f). Note the decrease in pond water level to 0 m by about day 200 (19 July). The curve derived from water level recorder measurements shows both a diurnal cycle and a distinct drop in head associated with drainage events. The asterisks in Figure 5d and E denote the composition of ice forming at the contact between fresh and seawater in under-ice melt ponds (false bottoms).

is less distinct, in particular since the drainage basins of individual ponds shrink with increasing ice permeability. For example, a melt pond located 0.1 m asl in 2 m thick ice of permeability  $4 \times 10^{-11} \text{ m}^2$ , would be in steady state for a surface ablation rate of  $17 \text{ mm d}^{-1}$  (WE) over a drainage basin 10 times as large as the pond area. While these numbers are typical of the early melt season, an increase in permeability by one order of magnitude to  $4 \times 10^{-10} \text{ m}^2$  results in a drop of hydraulic head to 0.01 m to maintain steady state, even if the drainage basin would not shrink. The change in volume associated with deepening of the pond through in situ melt can only account for a drop in water level by between 0.01 and 0.03 m over the entire melt season, while thinning of the ice would explain a reduction in pond head by up to 0.1 m between early June and late September.

[28] The impact of changes in permeability, which evolves gradually during the melt season, as compared to short-term variability in melt rates, has been monitored with a water-level recorder (sampling every 5 min.) mounted in a stilling well near the Atlanta mass balance site (Figure 5a, solid line). The data indicate that diurnal variations in surface melt rates, particularly pronounced under clear skies with nighttime freeze-back, account for daily oscillations in water level with amplitudes in the millimeter- to centimeter-range. These nighttime drops in pond level were associated with shrinkage of individual ponds. The trend of decreasing water level is punctuated by two distinct drainage events between days 191 and 193 (Figure 5a). The first of these could be linked to the opening of a permeable zone along the pond margin, resulting in rapid drainage that only subsided as water levels dropped below the outlet. Such drainage events had also been recorded in other melt ponds during the preceding weeks.

### 3.4. Vertical Transport and Percolation of Meltwater Into the Ice Cover

#### 3.4.1. Stable Isotope Tracers

[29] Most surface meltwater is produced within the snow cover and the uppermost 0.1 m of ice [Grenfell and Maykut, 1977], well above sea level. In a study of MY ice desalination, Untersteiner [1968] showed that the downward percolation of this meltwater reduces the salinity of the underlying ice, resulting in linear salinity profiles increasing from about 0 ‰ at the surface to  $>2$  ‰ at 1 m depth. Here, the vertical component of the meltwater flux has been tracked through repeated measurements of the isotopic composition ( $\delta^{18}\text{O}$ ) of the ice cover at 0.05 m vertical resolution. As shown in Table 1, the snow is highly depleted in  $^{18}\text{O}$  as compared to seawater and sea ice, the latter being enriched in the heavier isotope due to isotopic fractionation during ice growth [Eicken, 1998]. Thus the percolation of snow meltwater into the ice cover could be traced through its isotopic signature (Figure 6). Owing to the lower temperatures of the ice surface ( $-0.5$  to  $-1^\circ\text{C}$ ), snow meltwater refroze upon infiltration of the uppermost ice layers, resulting in the formation of clear, low-salinity superimposed ice, apparent both in the ice stratigraphy and the salinity and stable isotope profiles (Figure 6). As MY ice had already undergone one or several cycles of summer meltwater penetration, the infiltration pattern was more distinct in FY ice. Nevertheless, the widespread presence and recurring



**Table 1.** Depth or Thickness, Salinity (S),  $\delta^{18}\text{O}$ , and Fraction of Meteoric Water ( $f_{\text{met}}$ ) for Snow, Ice, and Pond Water at the SHEBA Site

Samples	Depth/Thickness, m		S, ‰		$\delta^{18}\text{O}$ , ‰		$f_{\text{met}}$ , %	n <sup>a</sup>
	Mean	Standard Deviation	Mean	Standard Deviation	Mean	Standard Deviation		
Snow	0.34 <sup>b</sup>	0.19	1.0	2.3	−23.2	5.3	100	46
Sea ice	1.77	0.62	4.5 <sup>c</sup>	2.6	−1.9 <sup>d</sup>	0.5	0	78
False-bottom ice	0.15	0.05	0.4	0.4	−10.1	3.7	33	35
Melt ponds								
1–15 June	0.11	0.06	0.3	0.9	−16.5	3.7	68	38
16–30 June	0.14	0.20	0.2	0.4	−9.7	5.2	36	8
1–15 July	0.14	0.08	0.3	0.8	−7.0	2.2	24	31
16–31 July	0.22	0.09	0.5	0.8	−4.3	1.0	11	24
1–7 Aug.	0.29	0.08	7.0	11.7	−4.2	0.8	11	18

<sup>a</sup>Number of isotope and salinity samples.<sup>b</sup>Data from *Perovich et al.* [1999b].<sup>c</sup>FY and MY ice at start of melt season.<sup>d</sup>Excluding layers infiltrated by meteoric water.

formation of such a low-permeability ice layer was of considerable importance in sealing off the ice surface and thus greatly reducing drainage of meltwater during the first two to three weeks of ice melt.

[30] During summer, the brine in the uppermost meter of the ice cover was gradually displaced by infiltrating snow and ice meltwater. From the salt balance (with an initial ice salinity of  $S_{i,0}$  and a salinity  $S_{i,t}$  at time  $t$ ) the amount of brine replaced by zero-salinity meltwater ( $m_f$ ) relative to the total brine volume  $m_b$  is given by

$$\frac{m_f}{m_b} = 1 - \frac{S_{i,t}}{S_{i,0}}. \quad (7)$$

The total fraction of meteoric water (snow or rain)  $f_m$  can be determined from the stable isotopic composition ( $\delta^{18}\text{O}$  of samples) as

$$f_m = \frac{\delta^{18}\text{O}(\text{sample}) - \delta^{18}\text{O}(\text{sea ice})}{\delta^{18}\text{O}(\text{meteoric}) - \delta^{18}\text{O}(\text{sea ice})}. \quad (8)$$

For the FY ice shown in Figure 6, 82% of the brine had been replaced by snow and ice meltwater by day 170 and more than 98% by day 194. A major fraction of the FY ice at the SHEBA site (observed at all FY sites with ice thicknesses of 1.4 m or less at the start of melt) was subject to convective overturning and replacement of brine in the lowermost 0.2

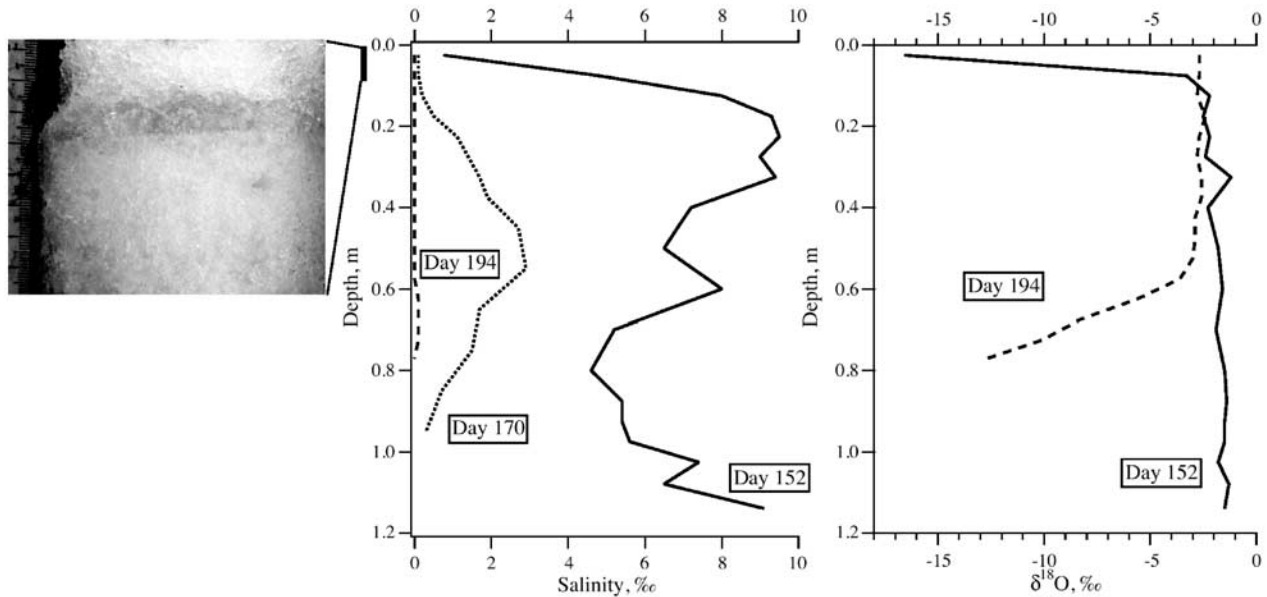


**Figure 6.** Texture (left; 0–0.08 m depth), salinity (center) and  $\delta^{18}\text{O}$  (right) profiles for cores taken from level FY sea ice near the Blue Bio site on 1 June, 19 June, and 13 July (days 152, 170, and 194). The stratigraphic core image as well as the stable isotope profile clearly show a layer of superimposed ice at the surface during the early melt season. By mid-July, a combination of percolation from the top down and displacement of brine through convective overturning from below has resulted in near-complete desalination of the ice cover.

to 0.5 m by underplating freshwater. Even toward the end of summer such meltwater still contained significant fractions of meteoric water (36% for the core shown in Figure 6, compared to a 20% meteoric fraction of total surface melt), indicating a compartmentalization and lack of mixing of the meltwater reservoir. Such meltwater segregation may have been promoted by a layer of newly grown ice sealing off freshwater lenses from the colder seawater underneath [Eicken, 1994]. Formation of such underwater ice or false bottoms was widespread at the SHEBA site, sealing off fresh or brackish water (with high fractions of meteoric water, as evident from the samples shown in Figures 5d and 5e, and Table 1) in depressions and cavities at the base of the ice cover. If at all, this water was only released through bottom melt and floe breakup later in the season, resulting in a delayed, pulsed input of freshwater into the mixed layer [Kadko, 2000].

### 3.4.2. Tracing Meltwater With $^7\text{Be}$

[31] Melt percolation is more difficult to detect in MY ice. The surface layers have already been transformed by melt events of previous summers, greatly limiting the utility of salinity and stable isotope tracers. This problem is amplified during the latter part of the melt season, when the isotopically depleted snow meltwater signal has been dissipated or immobilized in the ice cover. To overcome these problems, we have employed the transient tracer Beryllium-7. While  $^7\text{Be}$  concentrations are high in surface snow and ice meltwater, they tend toward zero in ice or brine that has not been exposed to the atmosphere. This is essentially confirmed by a vertical profile through level MY sea ice at the Pittsburgh site (Figure 7). In the deep interior of the ice,  $^7\text{Be}$  concentrations in brine collected from core holes are below 0.5 dpm  $\text{l}^{-1}$ , with a steady increase toward the surface of the ice cover. The vertical distribution of Beryllium in the brine can be simulated, assuming downward advection of  $^7\text{Be}$  deposited at the surface and average surface melt rates of  $0.02 \text{ m d}^{-1}$ . With the vertical advection velocity  $v_z$  derived from salinity and stable isotope data for FY ice (see above), the vertical profile of  $^7\text{Be}$  can be derived from the time-dependent decay with depth ( $t = z/v_z$ ):

$$^7\text{Be}(z) = ^7\text{Be}(z_0) \exp\left(-\lambda \frac{z}{v_z}\right), \quad (9)$$

with decay constant  $\lambda = 0.013 \text{ d}^{-1}$  [Kadko, 2000]. Despite some vertical mixing of brine during sampling, the model agrees well with the data, both in deeper layers isolated from the atmosphere during the ice growth season ( $\sim 250$  days old; see Figure 7) as well as in the uppermost, youngest layers (9 days old). Note that the isotopic composition of neither ice nor brine provides any indication of meltwater transport, while the transition between the upper, desalinated ice layers and the lower, pristine ice as indicated by the salinity profile matches the  $^7\text{Be}$  profile reasonably well. The results demonstrate that  $^7\text{Be}$ , as an atmospherically deposited tracer with a half-life that matches the characteristic timescales of summer percolation processes, is well suited for the study of meltwater transport within the ice cover.

### 3.4.3. Fluorescent tracers

[32] Rates of meltwater percolation have also been derived with the aid of fluorescent tracers. Figure 8 shows

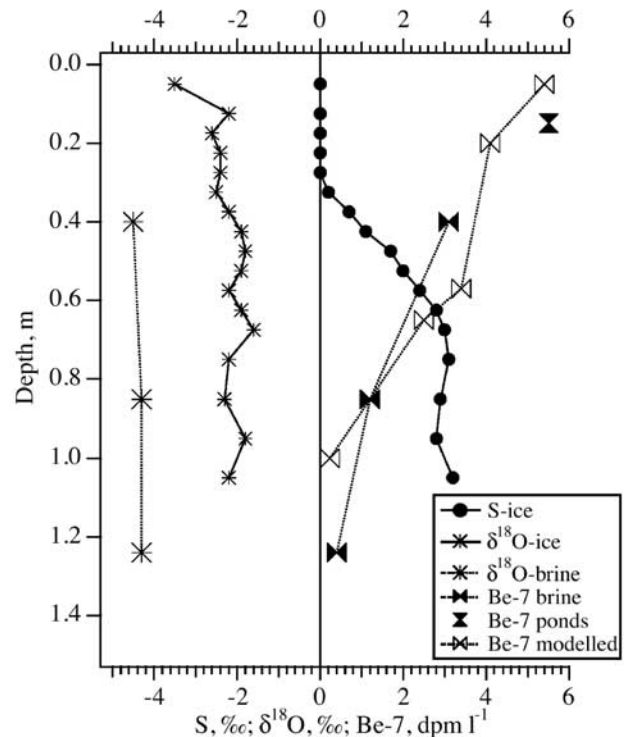


**Figure 7.** Penetration of surface meltwater into bare MY sea ice at the Pittsburgh site, as revealed in the  $^7\text{Be}$  signal recorded in brine sampled from different depths of the ice on 21 July (day 202), including an average of pond water samples. Note increase in  $^7\text{Be}$  toward surface and the lack of a similar trend in the  $\delta^{18}\text{O}$  data. Also shown are the salinity and  $\delta^{18}\text{O}$  of solid ice and brine.

results from an experiment with release of 4 g Rhodamine B (RB) over a  $0.5 \text{ m}^2$  area of level, MY white ice adjacent to topographic profile 1 (at 20 m along profile [see Eicken *et al.*, 2001, Figure 7]). Visual observations and core sampling 10 days after the initial release (with a corresponding surface melt of 0.15 m of ice) revealed that the tracer front had propagated roughly 0.25 m into the white ice. However, a significant fraction of the meltwater generated at the surface was advected horizontally through the uppermost, permeable ice layers into a neighboring melt pond. Owing to higher porosities and higher permeabilities of the pond ice, the tracer front had not only moved laterally by 4 m but also penetrated approximately 0.35 m into the ice at the pond bottom (0.65 m true depth; Figure 8). On 8 August, 19 days after the start of the experiment, the tracer maximum concentrations were found at 0.35 m depth in the white ice, whereas the signal had completely penetrated the pond ice with only traces of RB present. At the same time, the salinity of the uppermost 1 m of the white ice decreased significantly as a result of meltwater drainage and flushing. The pond ice, on the other hand, increased in salinity due to entrainment of seawater into the interconnected melt ponds (see section 3.5).

### 3.5. Lateral Meltwater Transport

[33] Owing to the low bulk ice permeabilities (Figure 3) and the development of an impervious layer of super-

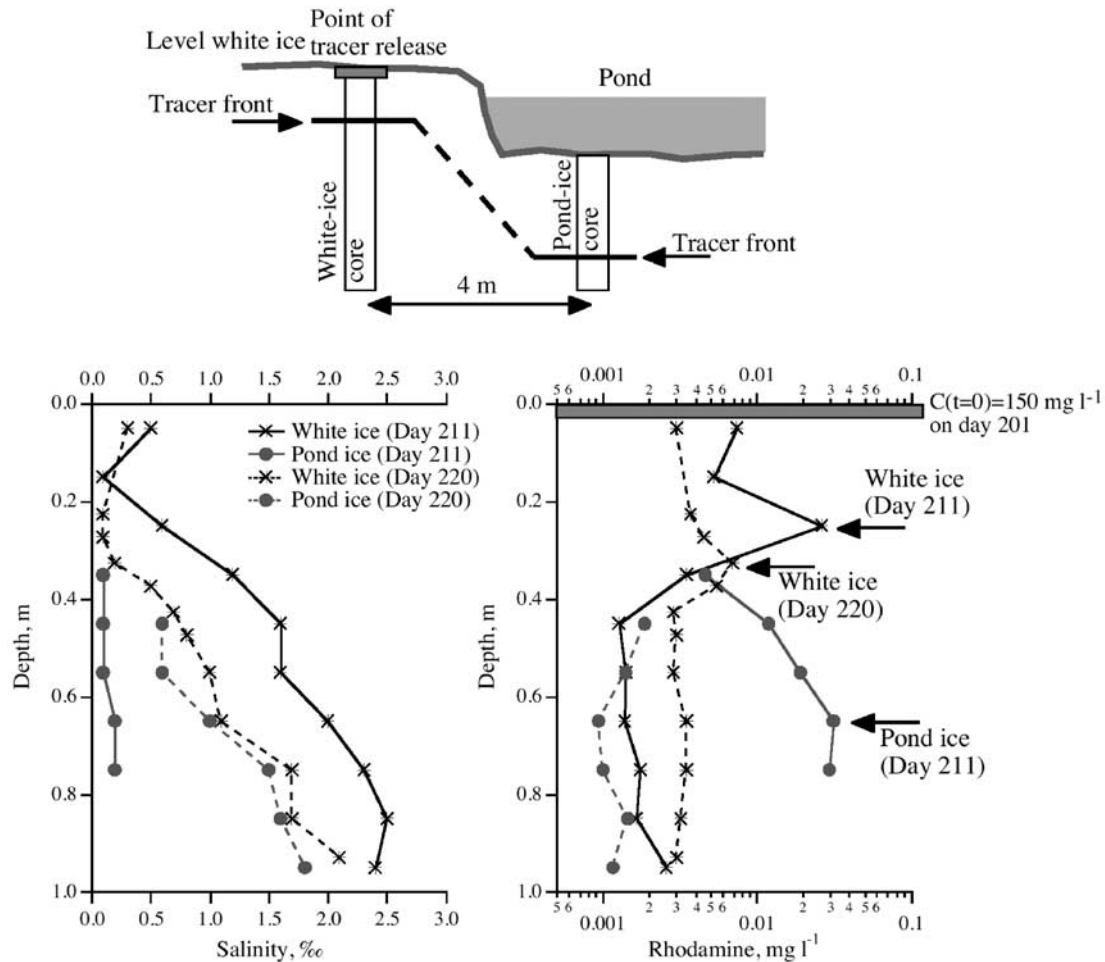


**Figure 8.** Meltwater movement as tracked after release of Rhodamine B at the surface of level, MY white ice on 20 July (day 201; see sketch at top).

imposed ice (Figure 6), a significant portion of the ice cover was inundated by a cm- to dm-thick layer of meltwater during the first two to three weeks of the melt season. Initially, most of this water was concealed in the snowpack. The movement of meltwater was traced in an area of level MY ice with surface slope  $<0.01$  (at 77 m along topographic profile 1 [see Eicken *et al.*, 2001, Figure 7]) through release of 500 mg of fluorescence on 16 June (day 167). After 29 hours, the tracer had been dispersed over an area approximately 3 m in radius, with the peak concentration at the center of the patch reduced by three orders of magnitude and advected 5 m away from the point of release. Such lateral meltwater dispersal was observed in all ice types and resulted in pooling of meltwater in topographic depressions, which in several cases could be shown to coincide with the location of previous summer's melt ponds [Eicken *et al.*, 2001].

[34] Bulk ice permeabilities were too low to support substantial drainage of meltwater during the early ablation season, but meltwater runoff was observed along floe margins and through flaws in the ice cover. Due to large floe sizes and wide spacing between leads at the SHEBA site, cracks of few centimeters to several decimeters width

were the most important sites of freshwater discharge in level ice [Richter-Menge and Perovich, 2001]. While such cracks refroze quickly during the cold season, they appeared to harbor more permeable, thinner ice opening up much earlier than the surrounding white-ice cover. Surface water drainage also contributed to an increase in permeability and widening of flaws due to the enhanced heat flux. Drainage through natural and artificial flaws (cracks at Atlanta and dive holes of 1 m diameter at Sediment City) was studied in more detail to quantify the amount and nature of surface runoff between days 170 and 190 when lateral flow was at a maximum. The drainage basin was mapped through sequential release of tracers in combination with surface topography measurements. The amount of runoff into the flaw was determined through measurements of the specific discharge. As the drainage patterns had been well established by day 170, the latter was mostly restricted to measurements in numerous flow channels draining into the flaw.

[35] Discharge into the water column underneath the ice at these locations averaged at  $45 \pm 28 \text{ m}^3 \text{ d}^{-1}$  (Figure 9, top), peaking at approximately  $100 \text{ m}^3 \text{ d}^{-1}$ . Typical drainage basins ranged between 1000 and 3000  $\text{m}^2$  in area



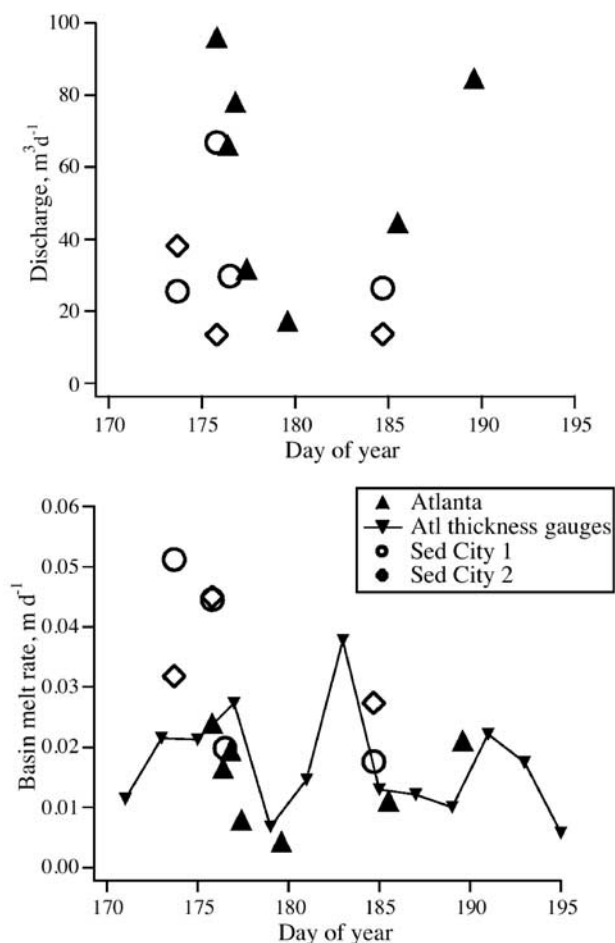


**Figure 9.** Discharge of surface meltwater through natural conduits (thermal crack at Atlanta) and artificial gauging holes (Sediment City locations, top) and surface melt rates (water equivalent, bottom) averaged over entire drainage basin, ranging between 300 and 4000 m<sup>2</sup> in area.

(minimum 300 m<sup>2</sup>, maximum 4000 m<sup>2</sup>). Based on drainage basin size and discharge, the amount of runoff per unit area can be determined (Figure 9, bottom). This yields basin-wide melt rates on the order of a few centimeters per day (average  $0.024 \pm 0.014$  m d<sup>-1</sup>) with substantial variations by as much as a factor of five over the course of a few days. These numbers compare well with 2- to 3-day average surface melt rates obtained with thickness gauges at Atlanta (Figure 9, bottom). Based on surface-energy balance measurements at the main SHEBA met tower, which show excellent agreement between melt and discharge maxima and peaks in the total energy flux at the ice surface [Persson *et al.*, 1999], it appears as if clear-sky, high incident short-wave flux conditions (over the course of one or several

days) are particularly effective in enhancing discharge of surface meltwater.

[36] Increasing ice permeability (Figure 3) and removal of the low-permeability surface layer (Figure 6) reduce the importance of lateral meltwater flow from late June onward. However, in areas of rough or ridged ice where hydraulic gradients can be much higher than in level ice, surface meltwater transport always plays an important role. This was investigated in a tracer experiment at the ridge site (Figure 10), where a system of melt ponds extended out for >10 m from the crest of the ridge with pond surfaces up to 0.54 m asl and surface slopes of up to 0.1. From the release point in a pond near the ridge crest (0.44 m asl), the tracer front moved by more than 6 m in 25 min, covering a total linear distance of approximately 16 m in 110 min and eventually draining into a pond at sea level. A significant fraction of the transport occurred below the ice surface, at the interface between the solid ice and a high-permeability, deteriorated surface layer clearly visible in Figure 10d.

[37] Time series of <sup>7</sup>Be concentrations in melt ponds between early July and early August (Figure 5f) provide further information about meltwater dispersion. Initially, <sup>7</sup>Be activity decreased because of melt input from older ice from the pond bottom and the drainage basin. However, the last two measurements on 7 and 8 August exhibit a distinct increase in <sup>7</sup>Be corresponding to a rise in pond salinity. The high <sup>7</sup>Be was derived from the formation of a highly stratified surface layer in adjacent leads formed from solar heating and meltwater input [Perovich *et al.*, 1999a; S. Pegau, unpublished data, 1998]. This layer, only 1.2 m in depth, concentrated <sup>7</sup>Be derived from atmospheric input (>3000 dpm l<sup>-1</sup>) (D. Kadko, unpublished data, 1998). Intensified wind mixing subsequently redistributed this <sup>7</sup>Be-rich surface water under the ice followed by entrainment into the melt ponds. With water temperatures of up to 2°C, porosity and permeability of pervious zones was further increased, promoting breakup and disintegration of floes.

### 3.6. Retention of Meltwater by False Bottoms in Under-Ice Ponds

[38] Apart from discharge off the sides, surface meltwater is released through localized flaws in the ice cover (section 3.5; Figure 9) as well as through wider zones of higher permeability such as pond bottoms (section 3.4; Figure 8). As a result of these processes, low-salinity meltwater comes into contact with seawater, each at or close to their respective freezing points. The temperature differential between the two water masses is sufficient to induce formation of underwater ice, a widespread occurrence at the SHEBA site. Initially, ice platelet crystals would form in the contact zone and grow to centimeter or decimeter size if attachment prevented their removal from the halocline. Subsequently, a more solid ice cover formed along the entire freshwater/seawater interface, stabilized by a mesh of crystals and other anchor points at the ice bottom. These slabs of underwater

**Figure 10.** (opposite) Photographs of tracer dispersal at flanks of ridge mass balance site. Upper panel (a) shows surface elevation (blue bars) and depth (red bars) of ponds at the site. Images in Figures 10b–10d were taken 25 min after release of tracer (marked by arrow in a and b). Core stratigraphy indicates that the bulk of the flow takes place in the upper ice layers below the highly porous, deteriorated layer visible at the top of the core (d). In 110 min the tracer front covered a linear distance of approximately 16 m from the point of release located 0.44 m asl down to the pond situated at sea level (Figure 10a, lower right).

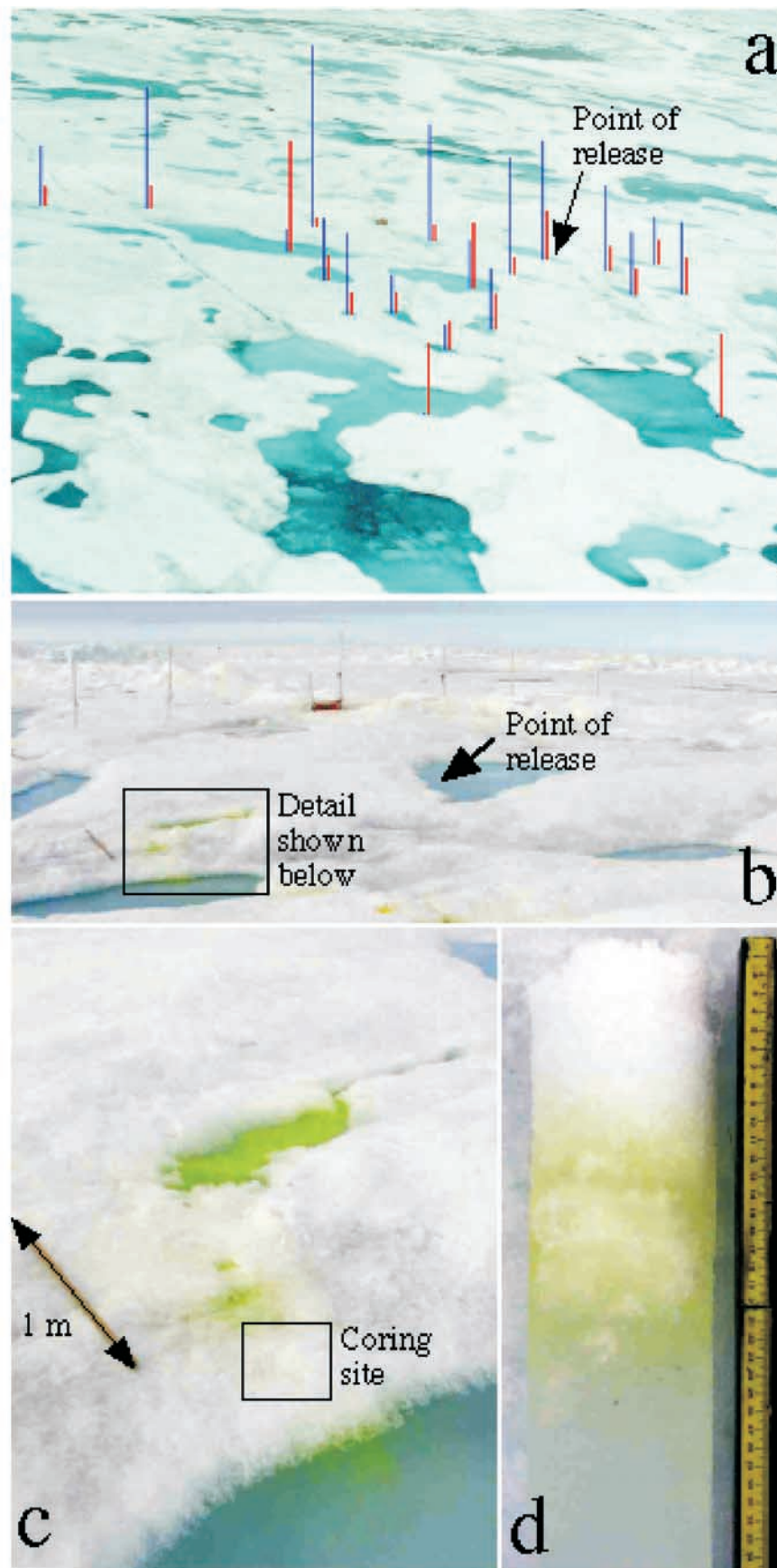


**Table 2.** Retention of Surface Snow and Ice Meltwater<sup>a</sup>

Reservoir	Ice Layer Thickness, m	Pond Depth, m	$V_b$ , %	$f_{met}$ , %	Melt Layer Thickness, m
Sea ice					
First-year ice	0.9		150	12	0.13
Multi-year ice	1		90	11	0.09
Pond ice	1.3		290	11	0.36
Surface melt ponds					
1 June to 15 July		0.14		24	0.03
16 July to 7 Aug.		0.29		11	0.06
Under-ice melt ponds					
1 June to 15 July	0.16	0.35		42	0.02 <sup>b</sup>
16 July to 7 Aug.	0.16	0.47		27	0.03 <sup>b</sup>
Total (1 June to 7 Aug.)					0.24 <sup>c</sup>

<sup>a</sup> Area-averaged melt layer thickness based on thickness of meltwater volume and volume fraction of liquid in ice  $V_b$ ;  $f_{met}$  denotes fraction of meteoric water.

<sup>b</sup> Based on areal fraction of 0.05.

<sup>c</sup> For sea ice, meltwater layer based on areal fractions of 0.7, 0.2 and 0.1 for bare MY ice, melt ponds and bare FY ice, respectively.

ice (false bottoms) could stretch horizontally for several meters and would effectively seal off depressions in the ice bottom filled with low-salinity meltwater, typically several decimeters deep (Table 2). Ice growth rates were on the order of several centimeters per day, with maximum false-bottom thicknesses of around 0.2 m (Table 1).

[39] While the importance of false bottoms for the heat and mass budget of the summer sea-ice cover is not the topic of this contribution, they play an important role as reservoirs of surface meltwater, retaining much higher fractions of meteoric water than surface melt ponds (Tables 1 and 2). Reliable assessments of their areal distribution and overall volume are quite difficult, not least because their formation is promoted by drilling holes through the ice cover. Away from the permanent installations, ice perforation was kept to a minimum, however, at the SHEBA site (see Eicken *et al.* [2001] on noninvasive measurement techniques) and is not deemed to significantly impact our estimates of underwater ice formation. Artificial drainage of elevated surface melt ponds in camp did result in the formation of false bottoms, with as much as 0.1 m of ice forming overnight after a drainage event. Similarly, any flaw or crack draining the surface during early melt produced false bottoms. In some cases, several of these formed below one another, separated by intermediate water layers of increasing salinity.

## 4. Discussion

### 4.1. Seasonal Evolution of Sea Ice Hydrology and Impact on the Large-Scale Heat and Mass Balance of the Ice Cover

[40] The data presented above demonstrate that the hydrological evolution of summer sea ice depends critically on the balance between meltwater production at the surface and the permeability structure of the underlying ice. The latter is controlled both by the pore microstructure as well as the size and distribution of larger flaws. These two factors not only determine the retention of snow and ice meltwater but they also assume a pivotal role in the ice heat and mass balance, as ice albedo during the melt season is largely determined by the areal coverage and depth of melt ponds [Maykut, 1986; Appel, 1988; Curry *et al.*, 1995; Tschudi *et al.*, 2001]. Figure 11 (top) indicates the pond

coverage at the SHEBA site determined from aerial photography by Perovich *et al.* [2002] and surface measurements along two profiles in level and deformed MY ice [Eicken *et al.*, 2001], which to a large extent match the evolution of large-scale ice albedo [Perovich *et al.*, 2002]. The time series is characterized by four phases (Figure 11, lower panels), with an increase toward a first sub-maximum in pond coverage by mid- to late June, followed by a reduction in areal coverage with a subsequent increase toward an absolute maximum of between 15 and 30%. The final decrease toward mid-August is mostly a result of pond freeze-up and snow deposition. It should be noted that Figure 11 is solely based on observations at the SHEBA site; magnitude and timing of changes in pond coverage may vary regionally and interannually [Fetterer and Untersteiner, 1998].

[41] Stage 1 (days 149 to 175) is characterized by intermediate surface ablation and meltwater production rates (1 to 10 mm d<sup>-1</sup>). Ice permeabilities were very low (<10<sup>-11</sup> to 10<sup>-12</sup> m<sup>2</sup>; Figure 3; section 3.2) due to lower temperatures in the ice interior and the development of an impervious layer in the contact zone between snow meltwater (temperatures > -0.1°C) percolating downward and refreezing at the ice surface (temperatures < -1.0°C at the start of the melt season; Figure 6). With limited percolation of meltwater into the ice, water pooled at the snow/ice interface and was transported over considerable distances following the surface topography (Figure 10) or driven by hydraulic gradients resulting out of spatially varying melt rates in level areas (section 3.5). As demonstrated by the significant differences between pond fractions over level and deformed MY ice (Figure 11, top), the topography of the ice plays a key role in either confining ponds to narrow, deep pools or allowing them to spread over a mostly level surface. These observations also suggest that the differences observed in the pond fractions over FY and MY ice [Fetterer and Untersteiner, 1998] can be explained by differences in surface topography. However, we found no evidence of opposite trends in seasonal changes of pond area over FY and MY (or level and deformed MY) ice as reported by Fetterer and Untersteiner [1998]. In part, this is due to the fact that FY ice at the SHEBA site occurred mostly in the form of refrozen leads and not as large floes



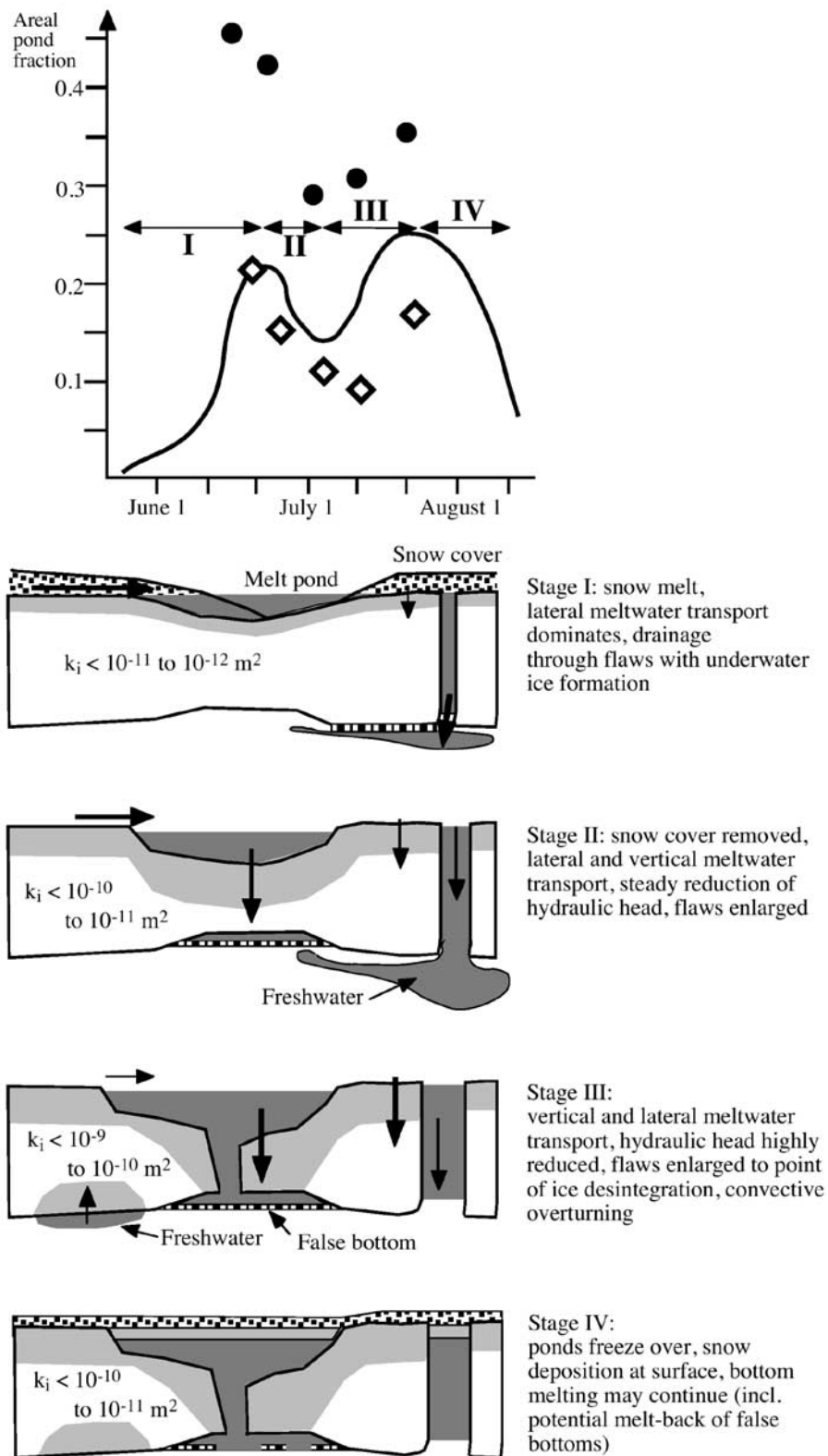


**Figure 11.** Temporal evolution of areal melt pond coverage and sea-ice hydrology at the SHEBA site. The thin line is based on aerial photography from *Perovich et al.* [2002]. Dots represent level MY ice (standard deviation in ice thickness along 100 m profile of 0.06 m asl, topographic profile 1 [*Eicken et al.*, 2001]), diamonds represent deformed MY ice (standard deviation in ice surface elevation along 60 m profile 0.18 m asl, topographic profile 2). Arrows in the upper panel denote the four different stages of ice melt.

such as those surveyed by the latter authors. The rapid increase in melt pond coverage and the corresponding decrease in ice surface albedo in early to mid-June were thus mostly driven by the removal of snow, exposing a meltwater layer that extended over significant stretches of the ice surface (Figure 11).

[42] At the SHEBA site, cracks (typically occurring at densities of a few cracks several tens of meters long per  $\text{km}^2$ ) were the most abundant feature supporting larger amounts of meltwater discharge into the underlying ocean during early melt (Figure 9). Formed in winter [Richter-Menge and Perovich, 2001], these cracks melted out earlier than surrounding ice, presumably due to higher salinities and lower albedos. As shown in section 4.2, the positive feedback of enhanced heat fluxes resulting out of flow focusing into these high-permeability zones contributed significantly to the opening of such flaws. Due to high hydraulic gradients (Figure 5a) and low ice permeabilities, many of the drainage networks visible in aerial photography (Figure 1) developed in the early melt season. Visual observations and repeat measurements along profiles through ponded ice demonstrated that such channel systems formed in early to mid-June tended to persist until the end of melt. Holt and Digby [1985, Figures 4f and 4h] report similar observations of drainage patterns developing around seal breathing holes and cracks in Arctic landfast sea ice.

[43] By 24 June, most snow, i.e., outside of ridged areas, had melted and the pond coverage approached a maximum. Ponds shrunk as bulk ice permeability increased and flaws draining into the ocean widened (as expressed through the reduction in pond surface elevation and hydraulic head; Figure 5a), despite overall increases in surface meltwater production (Figure 2). Thus, between 1 and 10 July, the majority of ponds surveyed at SHEBA had attained a surface height close to or at sea level. These events mark melt stage 2 (days 176 to 190).

[44] With hydraulic gradients driving much of the flow significantly reduced and with ice permeabilities increasing to above  $10^{-10} \text{ m}^2$ , the third stage of summer melt (days 191 to 207) was mostly characterized by vertical percolation of meltwater, with lateral transport limited to floe or pond margins (Figures 9 and 12) and deformed areas (Figure 10). Porous, permeable pond bottoms (Table 2) would still receive a significant flux of meltwater, contributing to deterioration and melting of ponded ice. Intrusion of meltwater was not limited to downward percolation, however. Freshwater build-up in leads combined with ongoing surface runoff resulted in pooling of warm freshwater underneath shallow-draft ice. Convective exchange contributes significantly to desalination and internal melting of the lower layers of sea ice (Figure 6; section 3.4). Increased melt pond coverage in late July and early August results at least in part from enhanced lateral heat fluxes into the permeable ice surrounding melt ponds, cracks and leads. During freeze-up (stage 4, day 208 onward) high ice permeabilities may still sustain significant advective fluxes of meltwater through the ice cover.

#### 4.2. Heat Fluxes Associated With Meltwater Transport and Decay of the Sea Ice Cover

[45] Melt ponds and surface water in leads can warm substantially due to solar heating during summer [Maykut

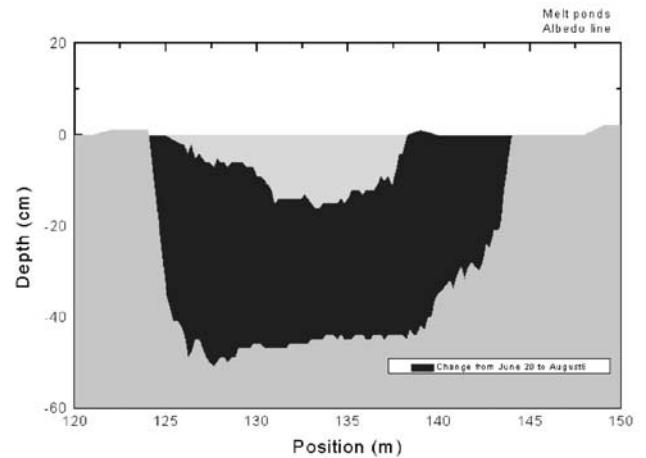


**Figure 12.** Cross section through a pond along albedo line (to the right of Quebec in Figure 1). The dark blue indicates the deepening and widening of the pond between 20 June and 8 August.

and McPhee, 1995; Perovich and Maykut, 1990]. The uppermost 1.3 m of leads surveyed at regular intervals at the SHEBA site had warmed to approximately  $2^\circ\text{C}$  (at a salinity of 2 psu) by early August [Perovich et al., 1999a; Pegau, unpublished]. While pond surface layers warmed up to  $1.2^\circ\text{C}$  on sunny days, mean water temperatures for the experiment documented in Figure 10 amounted to  $0.3^\circ\text{C}$ . In narrow channels or subglacial flow (Figure 10c), temperatures dropped to  $0^\circ\text{C}$ . For flow through the upper ice layer of thickness  $z_f = 0.2 \text{ m}$  (based on tracer distribution in ice cores; Figure 10d) and width  $w$ , and a temperature difference  $\Delta T = 0.3 \text{ K}$  between the local ice melting point and the water entering the ice margin of a pond, the heat flux can be derived as

$$\frac{dQ}{dt} = n_i c_p \rho_w z_f w v_f \Delta T. \quad (10)$$

With the specific heat of water  $c_p = 4.19 \times 10^3 \text{ J kg}^{-1} \text{ K}^{-1}$ , the density of water  $\rho_w = 1000 \text{ kg m}^{-3}$ , a percolation velocity  $v_f$  of  $1.7 \times 10^{-3} \text{ m s}^{-1}$  as derived from the tracer measurements and an ice porosity  $n_i$  of 0.15 the ice surrounding the pond receives a heat flux that would correspond to an input of  $64 \text{ W m}^{-2}$  at the ice surface (or  $320 \text{ W m}^{-2}$  across the pond wall). Compared to a net solar shortwave flux into the ice of  $100 \text{ W m}^{-2}$  [Persson et al., 1999], the magnitude of the advective heat flux is quite significant, at least in areas where hydraulic gradients or other driving forces such as wind stress help sustain fluid flow into ice neighboring a pond or lead. Such advective heat fluxes result in the formation and persistence of drainage features (Figure 10), but they also contribute to the widening of ponds during stage 3 of melt (Figures 11 and 12). For an average pond size of  $3 \times 10 \times 0.2 \text{ m}$ , a heat flux of  $50 \text{ W m}^{-2}$  (relative to the top ice surface) sustained for 12 hours a day into the downstream margin of the pond would result in an increase in pond coverage from 15% to 23% between 1 July and 1 August (assuming that radiative and turbulent fluxes would only deepen but not widen ponds), which is of the same order of magnitude as the changes observed at SHEBA [Perovich et al., 2002]. This is

also in fair agreement with the widening of individual ponds observed during the course of the summer, as demonstrated by the example shown in Figure 12. During a 49-day period, pond width increased by 6 m (at an average depth of 0.3 m), corresponding to an effective heat flux of  $210 \text{ W m}^{-2}$  through the pond walls or, referenced to the top ice surface, a heat flux of  $23 \text{ W m}^{-2}$  over the entire width of the retreating margin (ice density  $900 \text{ kg m}^{-3}$ ).

[46] Drainage of water through localized high-permeability zones or flaws in the ice cover during the early part of the melt season, when the surface layer does not sustain significant vertical percolation, results in even larger heat fluxes. For a discharge of  $50 \text{ m}^3 \text{ d}^{-1}$  (Figure 9) with  $\Delta T = 0.3 \text{ K}$  into a crack 0.2 m by 5 m wide and 2 m thick, filled with permeable, saline ice, the local heat flux exceeds  $700 \text{ W m}^{-2}$ , resulting in rapid melting and deterioration of the ice. Since the heat flow itself is proportional to the permeability of the ice matrix, localized melting is promoted by a positive permeability/heat-flux feedback, resulting in the preferred drainage of meltwater into high-permeability zones.

[47] While the heat flux associated with downward percolation of freshwater from the surface into the ice cover is mostly negligible ( $<0.2 \text{ W m}^{-2}$  for level white MY ice), convective overturning of freshwater pooling under the ice cover can contribute significantly to enlargement of pores and internal melt. This was observed along the margin of a lead (Sarah's Lake), which developed a 1.2 m thick freshwater layer with temperatures between 1 and  $2^\circ\text{C}$  and salinities between 0 and 5 psu during the course of the summer [Pegau, unpublished]. Once this water layer was thick enough to spread underneath stretches of level FY ice with drafts of around 0.9 m, convective overturning of brine resulted in desalination of the ice and enhanced internal melt, with pores enlarging to average diameters of several millimeters (Figure 6). Such high advective heat fluxes into more permeable pond-bottom and FY ice contributed significantly to the breakup and disintegration of the ice cover toward the end of the melt season (section 3.5; Figure 5). While FY ice grown in leads and cracks provides additional cohesion and contributes to the large-scale strength of the ice pack during the winter, its higher permeability (Figure 3; Table 2) and its susceptibility to infiltration with warmer meltwater from below during the summer months enhance the breakup and disintegration of the ice cover.

### 4.3. Retention of Surface Meltwater

[48] The distribution of surface meltwater between the different reservoirs toward the end of the melt season is indicated in Table 2. Of the total surface meltwater production of 0.59 m (WE), 61% were discharged into the mixed layer, while 39% were retained by the ice cover toward the end of the melt season (Table 2). Of the latter fraction, 26% were stored in surface melt ponds (based on mean pond depths and 20% areal coverage as derived from aerial surveys [Perovich *et al.*, 2002]), 13% in under-ice melt ponds, 30% in pond ice and the remainder in white ice (Table 2). Thus most of the meltwater associated with the ice cover resides within the pore space, displacing brine through vertical and lateral flow. In all shallow-draft FY sea ice at the SHEBA site (conservative estimate of 10% area, as compared to 15.8% derived from Radarsat Synthetic Aperture Radar data), underplating by freshwater induced convective

displacement of brine from the ice cover. Even in areas where density gradients or low permeabilities prevent convective overturning, diffusive exchange between the ice and the under-ice water layer can still result in significant freshwater fluxes [Eicken, 1994]. While uncertainties in the assessment of the large-scale areal extent of the fraction of FY and under-ice melt pond ice can be substantial (as high as 50%), the ensuing errors in freshwater retention are smaller due to the similarities between different ice types.

[49] The ice layer capping off under-ice melt ponds contains the highest fractions of snowmelt found in any of the reservoirs at the end of the ablation season. Since both the pond water and the false bottom can be entrained into the growing ice cover during the winter months, as observed by Jeffries *et al.* [1995] and Eicken [1994], this is an important mechanism of retaining a significant fraction of the snowmelt and associated atmospherically deposited pollutants in the sea-ice system, transferring them to the sites of maximum algal production at the floe bottom [Gradinger, 1996]. Whereas the thickest meltwater layers were found in under-ice melt ponds (Table 2), their contribution to the area-averaged meltwater layer thickness is small (13%) due to the comparatively small areal coverage estimated as 5%. Even at such low concentrations, under-water ice constitutes an important component of the net ice accretion and further work is needed to help us quantify their importance for the sea-ice mass balance, including the effects of late season bottom melt [cf. Untersteiner and Badgley, 1958].

[50] Some meltwater may be released through late-season bottom melt of false bottoms or disintegration of ponded floes not captured in this study. Furthermore, most of the 0.14 m of meltwater infiltrating the ice still displaces low-salinity fluid from the ice interior. Hence, over longer periods the 15% runoff deficit may only affect the mixed-layer salt balance in special cases. More importantly, however, this research has shown that the injection of surface meltwater into the mixed layer, at least at the SHEBA site, was not so much controlled by ablation rates but rather by the retention of meltwater on top of and under the ice. This explains the three-week delay between melt onset and appearance of a  $^7\text{Be}$  signal indicative of melt discharge in the SHEBA mixed layer [Kadko, 2000]. The retention of meltwater in unfrozen ponds and under-ice water layers furthermore implies a potential for significant discharge of freshwater into the mixed layer in late summer or fall. Phased entrainment could be triggered and promoted by autumn storms [cf. Yang *et al.*, 2001], advancing floe disintegration with subsequent pond drainage and melt of false bottoms.

### 4.4. Implications for Improvements in Atmosphere-Ice-Ocean Modeling

[51] One of the prime goals of the SHEBA Program is to improve models of atmosphere-ice-ocean interactive processes in the Arctic [Moritz *et al.*, 1993]. While this study cannot offer definitive conclusions along these lines, the major implications of our work (and potential ramifications) for ice modeling shall be briefly touched upon.

[52] It is well established that an adequate representation of ice albedo is a key requirement for realistic simulations of the Arctic ice pack. With the albedo of bare white ice



remarkably stable [Grenfell and Maykut, 1977; Perovich *et al.*, 2002], the summer ice albedo is mostly controlled by the depth and extent of melt ponds. Even the most sophisticated prognostic simulations of ice albedo [e.g., Schramm *et al.*, 1997; W. Lipscomb, unpublished data, 2000] currently prescribe one of these parameters (typically the seasonal evolution in areal extent as shown in Figure 11). As outlined in sections 3.1 to 3.3, the pooling of meltwater depends on the surface melt rates (currently well implemented in ice models provided that snowmelt is adequately considered), the hydraulic gradients driving flow (controlled by surface topography) and the permeability of the underlying ice. A fully prognostic, unconstrained simulation of ice albedo would thus need to include parameterizations or explicit derivations of these latter two parameters. Recent progress in predicting the evolution of ice roughness based on ice dynamic variables [Steiner *et al.*, 1999] may help in implementing ice surface elevation and morphology into large-scale numerical simulations. Given the stark contrasts between FY and MY ice in morphology and melt ponding (see Figure 11), even simple schemes may hold considerable promise.

[53] Adequate treatment of ice permeability is a challenging task. As shown above, on the scale of ponds meltwater diversion is determined by the macroscopic permeability of the ice matrix and the distribution and size of larger flaws (mostly cracks). The latter is determined by the build-up and release of thermal and dynamic stresses during the year and is indicative of “hidden” linkages between ice dynamics and thermodynamics [Richter-Menge and Perovich, 2001]. At this point, it may be quite reasonable, however, to assume some characteristic, constant distribution of cracks. The permeability of the ice matrix is highly variable over a range of scales, but could be parameterized in terms of the in situ porosity and a semiempirical geometric pore model [Freitag, 1999]. These difficulties are aggravated, however, by the fact that during the critical, early phase of melt, bulk ice permeability responds to the development of a thin, impervious layer at the contact between snow meltwater and the cold ice matrix (Figure 6). All of these questions extend well beyond the scope of this paper, but they clearly require further scrutiny.

[54] The ubiquity and magnitude of advective and convective heat transfer observed at the SHEBA site (potentially exceeding that of conductive and in some cases even of radiative transfer) suggests that meltwater transport may have to be taken into account in thermodynamic sea ice models, extending simulations beyond the simple one-dimensional approach. While simulations of bare white ice well removed from floe margins or ponds may not require such efforts, even here the vertical percolation of meltwater needs to be considered in more sophisticated models of ice growth and melt [e.g., Bitz and Lipscomb, 1999]. Meltwater flow through the ice matrix can substantially increase ice porosity (e.g., close to 30% in ice beneath ponds). Such internal melting may lead to little changes in ice thickness or albedo and hence needs to be properly resolved in large-scale models (e.g., parameterized as a function of ice type and thickness), where the residual of the surface energy balance (or solar heating of leads) is typically translated directly into changes in ice thickness or the fraction of open water. Preferential pooling of warm

meltwater under thinner FY ice also greatly promotes internal melting, but at the SHEBA site this went so far as to remove much of the thinner thicknesses classes (<1.5 m). As shown in section 4.2, the heat fluxes resulting out of such underplating are so substantial that they may well require revision of the common notion (and its manifestation in formulations of ice thickness distribution theory) that for a given albedo, the thickest ice classes experience the highest melt rates.

[55] As a final note of caution regarding the translation of measurements into model improvements, it needs to be pointed out that these observations depend to some degree on the specific location and timing of the SHEBA study. While observations in the Eurasian Arctic suggest that the extent and severity of melt are not necessarily unique [Eicken *et al.*, 1996; Haas and Eicken, 2001], in 1997 and 1998 the ice retreated substantially beyond the mean summer ice edge [Jeffers, 2001]. The reports from earlier ice camps indicate much less severe melt (<0.2 m surface ice melt at Station Alpha according to Untersteiner and Badley [1958]; preservation of superimposed ice formed early in the melt season as reported by Nazintsev [1963]) and it requires consistent observations extending over several melt seasons to help reduce potential bias in data sets transformed into model parameterizations.

## 5. Summary and Conclusions

[56] Despite the deceptively static image presented by a summer sea-ice cover, vertical and lateral fluxes of snow and ice meltwater are substantial and play a key role in the evolution of large-scale albedo, heat transfer and mass balance of the Arctic ice pack. Tracer studies and in situ ice permeability measurements showed that the seasonal progression of ice ablation and retention of meltwater are to a large extent controlled by the permeability of the ice cover. The macroscopic permeability varies by more than 2 orders of magnitude ( $<10^{-11}$  to  $>10^{-9}$  m<sup>2</sup>), mostly as a result of the gradual warming of the ice interior and the establishment of superimposed, impervious layers at the ice surface due to refreezing snowmelt. Meltwater production varies less overall (at maximum by one order of magnitude) but displays a more pronounced short-term variability which explains, e.g., diurnal oscillations in the level and extent of meltwater pooling at the ice surface. Further work is needed to determine the magnitude and fine structure of permeability in the critical surface layer since in situ measurements and tracer studies can only provide a limited assessment of the uppermost 0.1 to 0.2 m. The seasonal increase of ice permeability to values above  $10^{-10}$  to  $10^{-9}$  m<sup>2</sup> explains the widespread decrease in pond surface elevation and the concurrent reduction in hydraulic gradients driving fluid flow.

[57] The seasonal changes in ice permeability correspond to four distinct stages of melt. Stage 1 (days 149 to 175) is characterized by low ice permeabilities ( $<10^{-11}$  m<sup>2</sup>), resulting in widespread ponding, still concealed by the snow cover, and significant lateral transport of meltwater draining into cracks and other flaws. Up to 100 m<sup>3</sup> d<sup>-1</sup> were discharged from drainage basins several hundreds to thousands of square meters in size during this period. Increased heat flow due to meltwater discharge locally increased ice

permeabilities. Underwater ice formed at the points of contact between discharged freshwater and the underlying ocean, trapping meltwater at the bottom of the ice cover. Growing to more than 0.2 m thickness, the contribution of such ice to the total mass balance of the ice cover needs to be investigated in more detail. Under-ice ponds also constitute important snow meltwater reservoirs (25% meteoric water in late summer).

[58] With ice permeability increasing and hydraulic head decreasing during stage 2 (days 176 to 190) of the melt season, vertical percolation of meltwater becomes more important. By early July most ponds in level ice had equilibrated at sea level, resulting in shrinkage of pond area with concurrent increases in large-scale albedo of the ice [Perovich *et al.*, 2002]. In the ice, the meltwater front could be traced to 0.4–1 m depth toward the end of the season. The more permeable ice underneath ponds results in enhanced discharge into these areas, with freshwater collecting in bottom depressions, further promoting the development and sealing of under-ice melt ponds [Eicken, 1994].

[59] During stage 3 (days 191 to 207), increasing permeabilities and spreading of warmer freshwater from leads and cracks induced convective overturning of fluids in the lower half of FY floes, reducing salinities to values near zero and promoting internal melt and decay of the ice cover. At the same time, infiltration of warmer pond waters into surrounding ice (with heat fluxes up to several tens of  $W\ m^{-2}$ ) helped widen and deepen ponds with subsequent decreases in large-scale ice albedo. Meltwater-flow associated lateral heat fluxes were shown to be substantial and the localization of discharge greatly contributed or possibly controlled the disintegration and breakup of the ice cover. The linkages apparent between seasonal ice decay and meltwater flow are intriguing and worthy of further pursuit, in particular in the context of the wide and rapid retreat of the summer ice edge in the Arctic observed during recent years [Maslanik *et al.*, 1996; Jeffers, 2001]. Furthermore, this work indicates that models of ice growth and melt (currently almost exclusively representing these processes as one-dimensional) need to take into account internal melting driven by advective/convective heat fluxes as well as preferential melting in low-draft ice due to underplating by warm meltwater.

[60] Stage 4 (day 208 onward) marks the end of the melt season. Of the surface meltwater produced at the SHEBA site during the summer, roughly 40% remained associated with the ice cover in one of three reservoirs: surface ponds, under-ice melt ponds and false bottoms or meltwater percolating into the ice matrix. The latter constituted the largest single meltwater pool (based on an areal average), but it also displaced fluid from the ice, reducing the net meltwater retention to around 15%. While this signal is only of marginal importance for the long-term mixed-layer salt balance, punctuated release of freshwater from the ice cover, as controlled by hydrological and dynamic processes, can strongly impact the seasonal evolution of the surface ocean and needs to be considered in more detail. Retention of surface meltwater is also likely to promote the transfer of atmospheric pollutants to sea-ice biota.

[61] It is the balance between ice permeability and surface ablation rates that determines the extent and distribution of meltwater pooling at the surface of summer Arctic sea ice, thereby also affecting its large-scale albedo. Given the

potential importance of feedback processes and considering some of the recent changes observed in the state of the summer Arctic ice pack, it becomes imperative to understand and predict the processes that control the hydrology and plumbing system of the Arctic ice cover. As this study has shown, the large-scale ice permeability is not only controlled by the surface energy balance, but also by the distribution of flaws as well as the salinity and microstructure of the underlying ice. Future work will have to show whether these parameters are capable of amplifying or damping the response of the ice pack to climate variability and change.

[62] **Acknowledgments.** Support from the National Science Foundation Grants OPP-9872626 (H.E.) and OPP-9701067 (D.K.), Office of Naval Research Grant N00014-97-1-0765 (D.K.P.) and the Geophysical Institute at UAF is gratefully acknowledged. Field work could not have been accomplished without the help of the *Des Groseilliers*' crew, the SHEBA Project Office, and the SHEBA sea-ice team. Buster Welch is thanked for lively, insightful discussions, which led to his construction of a stilling-well gauge to record short-term variability in pond water level. Comments by Norbert Untersteiner, Florence Fetterer and an anonymous reviewer helped to improve the manuscript.

## References

- Appel, I. L., Features of thermal destruction of inhomogeneous ice cover, *Sov. Meteorol. Hydrol.*, 10, 65–71, 1988.
- Bauch, D., P. Schlosser, and R. G. Fairbanks, Freshwater balance and the sources of deep and bottom waters in the Arctic Ocean inferred from the distribution of  $H_2^{18}O$ , *Prog. Oceanog.*, 35, 53–80, 1995.
- Bitz, C. M., and W. H. Lipscomb, An energy-conserving thermodynamic model of sea ice, *J. Geophys. Res.*, 104, 15,669–15,677, 1999.
- Cooper, L. W., C. R. Olsen, D. K. Solomon, I. L. Larsen, R. B. Cook, and J. M. Grebmeier, Stable isotopes of oxygen and natural and fallout radionuclides used for tracing runoff during snowmelt in an Arctic watershed, *Water Resour. Res.*, 27, 2171–2179, 1991.
- Curry, J. A., J. L. Schramm, and E. E. Ebert, Sea ice-albedo climate feedback mechanism, *J. Clim.*, 8, 240–247, 1995.
- Dibb, J. E., Beryllium-7 and lead-210 in the atmosphere and surface snow over the Greenland ice sheet in the summer of 1989, *J. Geophys. Res.*, 95, 22,407–22,415, 1990.
- Eicken, H., Structure of under-ice melt ponds in the central Arctic and their effect on the sea-ice cover, *Limnol. Oceanogr.*, 39, 682–694, 1994.
- Eicken, H., Factors determining microstructure, salinity and stable isotope composition of Antarctic sea ice: Deriving modes and rates of ice growth in the Weddell Sea, in *Antarctic Sea Ice Physical Processes, Interactions and Variability*, *Antarct. Res. Ser.*, vol. 74, edited by M. O. Jeffries, pp. 89–122, AGU, Washington, D.C., 1998.
- Eicken, H., M. Lensu, M. Leppäranta, W. B. Tucker III, A. J. Gow, and O. Salmela, Thickness, structure and properties of level summer multi-year ice in the Eurasian sector of the Arctic Ocean, *J. Geophys. Res.*, 100, 22,697–22,710, 1995.
- Eicken, H., R. Gradinger, B. Ivanov, A. Makshtas, and R. Pác, Surface melt puddles on multiyear sea ice in the Eurasian Arctic, in *World Climate Research Programme WCRP-94, Proceedings of the ACSYS Conference on the Dynamics of the Arctic Climate System* (Göteborg, Sweden, 7–10 November 1994), *WMO/TD Rep. 760*, edited by P. Lemke, L. Anderson, and R. G. Barry, pp. 267–271, World Meteorol. Org., Geneva, 1996.
- Eicken, H., W. B. Tucker III, and D. K. Perovich, Indirect measurements of the mass balance of summer Arctic sea ice with an electromagnetic induction technique, *Ann. Glaciol.*, 33, 194–200, 2001.
- Fetterer, F., and N. Untersteiner, Observations of melt ponds on arctic sea ice, *J. Geophys. Res.*, 103, 24,821–24,835, 1998.
- Freeze, R. A., and J. A. Cherry, *Groundwater*, Prentice Hall, Old Tappan, N.J., 1979.
- Freitag, J., The hydraulic properties of Arctic sea ice—Implications for the small-scale particle transport (in German), *Ber. Polarforsch.*, 325, 150 pp., 1999.
- Golovin, P. N., S. V. Kochetov, and L. A. Timokhov, Freshening of the underice layer due to melting, *Oceanology*, 35, 482–487, 1996.
- Gradinger, R., Occurrence of an algal bloom under Arctic pack ice, *Mar. Ecol. Progr. Ser.*, 131, 301–305, 1996.
- Grenfell, T. C., and G. A. Maykut, The optical properties of ice and snow in the Arctic Basin, *J. Glaciol.*, 18, 445–463, 1977.

- Haas, C., and H. Eicken, Interannual variability of summer sea ice thickness in the Siberian and central Arctic under different atmospheric circulation regimes, *J. Geophys. Res.*, **106**, 4449–4462, 2001.
- Holt, B., and S. Digby, Processes and imagery of first-year fast sea ice during the melt season, *J. Geophys. Res.*, **90**, 5045–5062, 1985.
- Jeffers, S., Investigating the anomalous sea-ice conditions in the Canadian High Arctic (Queen Elizabeth Islands) during summer, 1998, *Ann. Glaciol.*, **33**, 507–512, 2001.
- Jeffries, M. O., K. Schwartz, K. Morris, A. D. Veazey, H. R. Krouse, and S. Cushing, Evidence for platelet ice accretion in Arctic sea ice development, *J. Geophys. Res.*, **100**, 10,905–10,914, 1995.
- Kadko, D., Modeling the evolution of the Arctic mixed layer during the fall, 1997 Surface Heat Budget of the Arctic Ocean (SHEBA) Project using measurements of  $^7\text{Be}$ , *J. Geophys. Res.*, **105**, 3369–3378, 2000.
- Kadko, D., and D. Olson, Be-7 as a tracer of surface water subduction and mixed layer history, *Deep Sea Res.*, **43**, 89–116, 1996.
- Käß, W., Hydrogeological tracer techniques in waste remediation (in German), *Geowissenschaften*, **7**, 194–205, 1992.
- Krembs, C., R. Gradinger, and M. Spindler, Implications of brine channel geometry and surface area for the interaction of sympagic organisms in Arctic sea ice, *J. Exp. Mar. Biol. Ecol.*, **243**, 55–80, 2000.
- Lange, M. A., and S. L. Pfirman, Arctic sea ice contamination: Major characteristics and consequences, in *Physics of Ice-Covered Seas*, vol. 2, edited by M. Leppäranta, pp. 651–681, Univ. of Helsinki, Helsinki, 1998.
- Leppäranta, M., and T. Manninen, The brine and gas content of sea ice with attention to low salinities and high temperatures, *Internal Rep. 88-2*, Finn. Inst. Mar. Res., Helsinki, 1988.
- Martin, S., and P. Kauffman, The evolution of under-ice melt ponds, or double diffusion at the freezing point, *J. Fluid Mech.*, **64**, 507–527, 1974.
- Maslanik, J. A., M. C. Serreze, and R. G. Barry, Recent decreases in Arctic summer ice cover and linkages to atmospheric circulation anomalies, *Geophys. Res. Lett.*, **23**, 1677–1680, 1996.
- Maykut, G. A., The surface heat and mass balance, in *The Geophysics of Sea Ice*, edited by N. Untersteiner, pp. 395–463, Martinus Nijhoff, Zoetermeer, Netherlands, 1986.
- Maykut, G. A., and M. G. McPhee, Solar heating of the Arctic mixed layer, *J. Geophys. Res.*, **100**, 24,691–24,703, 1995.
- Moritz, R. E., J. A. Curry, A. S. Thorndike, N. Untersteiner, SHEBA: A research program on the surface heat budget of the Arctic Ocean, Appl. Phys. Lab., Univ. of Wash., Seattle, 1993.
- Nazintsev, Y. L., Role of thermal processes in ice melting and in modification of the relief of polar-ice floes in the central Arctic (in Russian), *Probl. Ark. Antark.*, **12**, 69–75, 1963.
- Nazintsev, Y. L., Evaluation of lateral melting of drifting ice floes (in Russian), *Tr. Ark. Antark. Nauchno-Issled. Inst.*, **303**, 180–184, 1971.
- Östlund, H. G., and G. Hut, Arctic Ocean water mass balance from isotope data, *J. Geophys. Res.*, **89**, 6373–6381, 1984.
- Perovich, D. K., Optical properties of sea ice, in *Physics of Ice-Covered Seas*, vol. 1, edited by M. Leppäranta, pp. 195–230, Univ. of Helsinki, Helsinki, 1998.
- Perovich, D. K., and G. A. Maykut, Solar heating of a stratified ocean in the presence of an ice cover, *J. Geophys. Res.*, **95**, 18,233–18,245, 1990.
- Perovich, D. K., et al., Year on ice gives climate insights, *Eos Trans. AGU*, **80**, 481, 1999a.
- Perovich, D. K., T. C. Grenfell, B. Light, J. A. Richter-Menge, M. Sturm, W. B. Tucker III, H. Eicken, G. A. Maykut, and B. Elder, *SHEBA: Snow and Ice Studies* [CD-ROM], Cold Reg. Res. and Eng. Lab., Hanover, N.H., 1999b.
- Perovich, D. K., T. C. Grenfell, and B. Light, Seasonal evolution of the albedo of multiyear Arctic sea ice, *J. Geophys. Res.*, **107**, doi:10.1029/2000JC000438, in press, 2002.
- Persson, P. O. G., E. L. Andreas, C. W. Fairall, P. S. Guest, and D. R. Ruffieux, The surface energy budget during the onset of the melt season on the Arctic icepack during SHEBA, in *Fifth Conference on Polar Meteorology and Oceanography of the American Meteorological Society, Dallas, TX, 10–15 January 1999*, pp. 321–326, Am. Meteorol. Soc., Boston, Mass., 1999.
- Richter-Menge, J. A., and D. K. Perovich, Summer ice dynamics during SHEBA and its effect on the ocean heat content, *Ann. Glaciol.*, **33**, 201–206, 2001.
- Romanov, I. P., *Atlas of Ice and Snow of the Arctic Basin and Siberian Shelf Seas*, 2nd ed., Backbone Publ. Co., New York, 1995.
- Schramm, J. L., M. M. Holland, J. A. Curry, and E. E. Ebert, Modeling the thermodynamics of a sea ice thickness distribution, 1, Sensitivity to ice thickness resolution, *J. Geophys. Res.*, **102**, 23,079–23,091, 1997.
- Silker, W. B., Beryllium and fission products in the GEOSECS II water column and applications of their oceanic distributions, *Earth Planet. Sci. Lett.*, **16**, 131–137, 1972.
- Steiner, N., M. Harder, and P. Lemke, Sea-ice roughness and drag coefficients in a dynamic-thermodynamic sea-ice model for the Arctic, *Tellus, Ser. A*, **51**, 964–978, 1999.
- Tschudi, M. A., J. A. Curry, and J. A. Maslanik, Airborne observations of summertime surface features and their effect on surface albedo during FIRE/SHEBA, *J. Geophys. Res.*, **106**, 15,335–15,344, 2001.
- Untersteiner, N., Natural desalination and equilibrium salinity profile of perennial sea ice, *J. Geophys. Res.*, **73**, 1251–1257, 1968.
- Untersteiner, N., Structure and dynamics of the Arctic Ocean ice cover, in *The Arctic Ocean Region*, edited by A. Grantz, L. Johnson, and J. F. Sweeney, pp. 37–51, Geol. Soc. of Am., Boulder, Colo., 1990.
- Untersteiner, N., and F. I. Badgley, Preliminary results of thermal budget studies on Arctic pack ice during summer and autumn, *Natl. Res. Council. Publ.*, **598**, 85–92, 1958.
- Yanes, A. V., Melting of snow and ice in the central Arctic (in Russian), *Probl. Ark. Antark.*, **11**, 59–64, 1962.
- Yang, J., J. Comiso, R. Krishfield, and S. Honjo, Synoptic storms and the development of the 1997 warming and freshening event in the Beaufort Sea, *Geophys. Res. Lett.*, **28**, 799–802, 2001.
- Young, J. A., and W. B. Silker, Aerosol deposition velocities on the Pacific and Atlantic Oceans calculated from  $^7\text{Be}$  measurements, *Earth Planet. Sci. Lett.*, **50**, 92–104, 1980.
- H. Eicken, Geophysical Institute, University of Alaska Fairbanks, Fairbanks, AK 99775-7320, USA. (hajo.eicken@gi.alaska.edu)
- H. R. Krouse, Department of Physics and Astronomy, University of Calgary, Calgary, Alberta T2N 1N4, Canada. (krouse@acs.ucalgary.ca)
- D. Kadko, Rosenstiel School of Marine and Atmospheric Sciences, University of Miami, Miami, FL 33149, USA. (dkadko@rsmas.miami.edu)
- D. K. Perovich, Cold Regions Research and Engineering Laboratory, Hanover, NH 03755, USA. (perovich@crrel.usace.army.mil)